

Phonon spectrum and correlations in a transonic flow of an atomic Bose gas

Florent Michel¹ and Renaud Parentani¹

¹*Laboratoire de Physique Théorique, CNRS, Univ. Paris-Sud, Université Paris-Saclay, 91405 Orsay, France*

(Dated: December 3, 2024)

Motivated by a recent experiment of J. Steinhauer, we reconsider the properties of the phonons spontaneously emitted in stationary transonic flows. The latter are described by “waterfall” configurations which form a one-parameter family of stable flows. For parameters close to their experimental values, in spite of high gradients near the sonic horizon, the spectrum is accurately planckian in the relevant frequency domain, where the temperature differs from the relativistic prediction by less than 10%. We then study the density correlations across the sonic horizon and the non-separable character of the final state. We show that the relativistic expressions provide accurate approximations when the initial temperature is not too high. We also show that the phases of the scattering coefficients introduce a finite shift of the location of the correlations which was so far overlooked. This shift is due to the asymmetry of the near-horizon flow, and persists in the dispersion-less regime.

CONTENTS

I. Introduction	2
II. Spontaneous emission of phonons in transonic flows	2
A. Parametrization of the background flows	2
B. Spontaneous emission of phonons, generalities	5
C. Spectral properties in waterfall background flows	7
III. The two-point correlation function	10
A. Generalities	10
B. Strength of correlations and their relativistic pattern	11
C. Non-separability	12
D. Phase of uu correlations	13
IV. Conclusion	14
Acknowledgments	15
A. Non-polynomial Schrödinger equation	15
1. Waterfall solutions	16
2. Equation on linear perturbations	17
B. Stability of the waterfall solutions	18
C. Shift of the correlations for a relativistic field	20
1. Relativistic shift of the maximum of G_2	20
2. The tanh case	22
3. Perturbed tanh profile	23
4. Linear profile	24
D. Phase of the coefficients α_ω and β_ω	25
References	26

I. INTRODUCTION

In a recent work [1], J. Steinhauer reported the observation of the spectrum and correlations of phonons emitted in a flowing condensed atomic gas [2]. The flow was transcritical, which means that there is a sonic horizon, and, to a good approximation, stationary. On a qualitative level, the observed properties agree rather well with the predictions one can draw from the analogy with black hole radiation pointed out by Unruh [3]. First, on the subsonic side, one expects to find a steady flux of phonons with a spectrum approximatively thermal and with a temperature given by the analog surface gravity, at least when the healing length is much smaller than the scale of the horizon surface gravity [4–8]. Second, in spite of dispersive effects which affect the early propagation, one expects that each of these quanta comes from a pair of entangled phonons, the partners carrying negative energy and propagating on the other side of the sonic horizon [5]. Two important features have been observed in [1]. On the one hand, near the sonic horizon, the background flow was observed to be close to a “waterfall” solution [9] with a high Mach number in the supersonic region $M_+ \approx 5$.¹ On the other hand, the initial temperature was reported to be low enough so that the initial state can be considered to be the incoming vacuum. Hence the phonons should be mainly emitted by spontaneous amplification of vacuum fluctuations, rather than stimulated by pre-existing ones (as is the case when working at a significant temperature). In fact, from the observation of density-density perturbations [10, 11], J. Steinhauer also reported that, for large frequencies, the intensity of the correlations fulfills an inequality which implies that the final phonon state is non-separable, as is the case when the spontaneous channel is the dominant one [12–17].

When working in vacuum and with background flows described by waterfall solutions, the spectral properties and coherence of the emitted phonons can be accurately determined by numerical methods. To this end, in this paper, we solve the Bogoliubov-de Gennes equation in these flows, focusing on the one with a Mach number $M_+ = 5$ in the supersonic region. To test the sensitivity of the predictions, we also consider nearby flows with $M_+ = 5(1 \pm 0.25)$. Despite their high spatial gradients (which are larger than the inverse healing length evaluated at the sonic horizon), we shall see that the spectrum accurately follows the Planck law in the relevant low frequency domain. We also observe that the scattering coefficients involving the co-propagating mode [7, 18] are about 10 times smaller than the coupling between the two counter-propagating modes carrying opposite energy (encoding the analogue Hawking effect [3, 4]). Hence, to a fairly good approximation, the spectral properties can be accounted for by their relativistic expression. This stops to be true when the initial temperature of the condensate is much higher than the Hawking temperature fixed by the surface gravity.

We then study the correlations between the phonons emitted on opposite sides of the sonic horizon. We find that the norm and the phase of the Fourier components of the term encoding these correlations are also well approximated by their relativistic expressions. Moreover, the weakness of the couplings to the co-propagating mode preserves the non-separable character of the final state for relatively high initial temperatures of the condensate. Focusing on the *phase* of this term, we find that its dependence on the frequency induces a non trivial shift of the locus of the correlations with respect to the expression of [10]. Interestingly, this shift persists in the relativistic limit when sending to zero the healing length. It originates from the large asymmetry of the background flow when crossing the sonic horizon.

The paper is organized as follows. In Section II, we first review the basic properties of waterfall solutions and the calculation of the scattering coefficients of linear density perturbations. We then analyze the spectral properties of the emitted phonons on waterfall flows with $M_+ \approx 5$. In Section III, we study the strength of the correlations of the phonon pairs in the same flows. We conclude in Section IV. In Appendix A, we study the waterfall solutions of the non-polynomial Schrödinger equation and compute the corresponding effective temperature of the emitted phonons. In Appendix B we report numerical results concerning the stability of the waterfall solutions of the GPE. Finally, Appendix C is devoted to the shift of the maximum of the two-point function in relativistic settings, whereas Appendix D focuses on the phase of individual scattering coefficients.

II. SPONTANEOUS EMISSION OF PHONONS IN TRANSONIC FLOWS

A. Parametrization of the background flows

To describe the background flows, we consider a 1-dimensional, dilute, weakly interacting atomic Bose-Einstein condensate (BEC) with repulsive interactions [2]. In the mean field approximation, the condensed atoms are described

¹ The values of the condensate velocity v and sound speed c reported in [1] seem to indicate that the condensate does not accurately satisfy the one dimensional Gross-Pitaevskii equation. Indeed, for any stationary solution, the product c^2v is a constant, while it varies by $\sim 50\%$ when using the reported values. This discrepancy could be (at least partially) explained by the three-dimensional character of the flow. These effects can be taken into account by using a generalized version of the Gross-Pitaevskii equation, see Appendix A.

by a complex field $\psi(t, x)$ which satisfies the Gross-Pitaevskii equation (GPE):

$$i\hbar\partial_t\psi = -\frac{\hbar^2}{2m}\partial_x^2\psi + V(x)\psi + g\psi^*\psi^2. \quad (1)$$

Here V is the external potential and g the two-body coupling. We assume that g is a constant and that V only contains the sharp potential drop engendering the sonic horizon. In other terms we neglect the shallow harmonic potential used in the experiment [1]. In this approximation, V only depends on x in the frame at rest with respect to the sharp potential.

To reduce the number of parameters, it is useful to define the non-dimensional quantities $\bar{x} \equiv x/X$, $\bar{t} \equiv t/T$, $\bar{\psi}(\bar{x}, \bar{t}) \equiv \psi(x, t)/\sqrt{\rho_0}$, $\bar{V}(\bar{x}) \equiv (mX^2/\hbar^2)V(x)$, and $\bar{g} \equiv (m\rho_0 X^2/\hbar^2)g$, where X and ρ_0 are two (so far arbitrary) strictly positive numbers, and where $T = X^2m/\hbar$. In the following we will only work with these dimensionless quantities. In this system, the healing length $\xi \equiv \hbar/\sqrt{mg\rho}$ (where $\rho = \psi^*\psi$ is the mean atomic density) becomes $\xi = 1/\sqrt{\bar{g}\bar{\rho}}$. As there is no ambiguity, from now on, we shall remove the bars to avoid cumbersome notations. The GPE then becomes

$$i\partial_t\psi = -\frac{1}{2}\partial_x^2\psi + V(x)\psi + g\psi^*\psi^2. \quad (2)$$

We look for stationary solutions of the form

$$\psi(x, t) = \sqrt{\rho(x)} \exp\left(i \int_0^x v(y) dy\right), \quad (3)$$

where ρ and v are two real-valued functions. (Note that a non-zero frequency can be absorbed into an additive constant to V .) Plugging this ansatz into Eq. (2) and taking the imaginary part gives the conservation of the current $\partial_x(\rho v) = 0$. Setting the scale X to have $J \equiv \rho v = 1$, the real part of Eq. (2) becomes

$$\frac{1}{2}\partial_x^2(\rho^{1/2}) = V\rho^{1/2} + g\rho^{3/2} + \frac{1}{2\rho^{3/2}}. \quad (4)$$

As a simple model of the sharp variation of the potential used in [1], we consider a step-like potential of the form

$$V(x) = \begin{cases} V_- & x < 0 \\ V_+ & x > 0 \end{cases}, \quad (5)$$

where $(V_+, V_-) \in \mathbb{R}^2$. In what follows, the subscript \pm denotes the sign of x . In general, integrating Eq. (4) over x in a region of homogeneous potential gives the square of $\partial_x\rho$ as a polynomial of degree 3. In our case we have two polynomials: one defined on the positive half-line and one on the negative half-line. We now focus on “waterfall” solutions [9]. Since these solutions are asymptotically uniform on both sides, the two integration constants must be chosen so that each polynomial has a double root:

$$(\partial_x\rho)^2 = 4g(\rho(x) - \rho_{1,\pm})^2(\rho(x) - \rho_{2,\pm}), \quad (6)$$

where the constants $\rho_{1,\pm}$, $\rho_{2,\pm}$ obey $2\rho_{1,\pm} + \rho_{2,\pm} = -2V_\pm/g$ and $\rho_{1,\pm}^2\rho_{2,\pm} = 1/g$. $\rho_{1,\pm}$ is the asymptotic value of ρ at $x \rightarrow \pm\infty$, while $\rho_{2,-}$ is the density at the bottom of the (unique) stationary soliton solution in the left region [19]. A waterfall solution is obtained by matching a uniform configuration $\rho = \rho_{1,+}$ for $x > 0$ with a half-soliton in the region $x < 0$. This solution thus requires $\rho_{2,-} = \rho_{1,+}$, which we set to unity by fixing the constant ρ_0 to be equal to $\rho_{1,+}$.

The solution is then *completely* determined by the value of $\rho_{1,-}$, which fixes all the other quantities, namely $g = \rho_{1,-}^{-2}$, $V_+ = -g(2 + \rho_{2,+})/2$, $V_- = -g(2\rho_{1,-} + 1)/2$, and $\rho_{2,+} = \rho_{1,-}^2$. (Note that this also fixes the sign of the discontinuity in V as $V_+ - V_- = -g(\rho_{1,-} - 1)^2/2 < 0$.) The asymptotic values of the Mach number ($M(x) \equiv v(x)/c(x) = \rho_{1,-}/\rho(x)^{3/2}$) are then $M_+ = M(x \rightarrow +\infty) = \rho_{1,-}$ and $M_- = \rho_{1,-}^{-1/2}$. Since the waterfall solution is supersonic for $x \rightarrow +\infty$, this imposes $\rho_{1,-} > 1$, i.e., $V_- < -1.5g$.

In brief, when working in our non-dimensional units with a uniform g and a step-like V , there is a one-parameter family of waterfall solutions parametrized by $\rho_{1,-} = M_+ > 1$. Returning to usual units, for a given type of atoms, the independent parameters can be taken to be the density $\rho_{1,-}$ and the depth of the potential $V_+ - V_-$. When requiring that the solution be stationary and asymptotically homogeneous, the current J is fixed. Explicitly, in our units, these solutions read

$$\rho(x) = \begin{cases} \rho_{1,-} + (1 - \rho_{1,-})(\cosh(\sigma x))^{-2} & x \leq 0 \\ 1 & x \geq 0 \end{cases}, \quad (7)$$

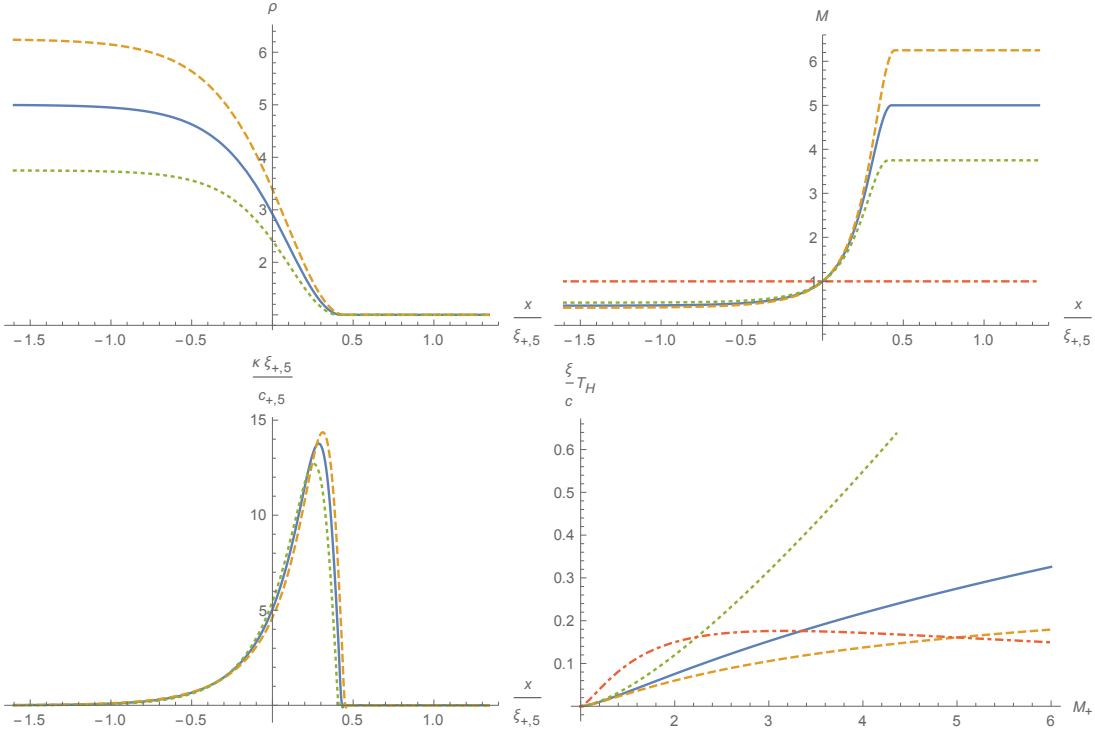


Figure 1. Plots of the atomic density (top, left) and the Mach number (top, right) for three waterfall solutions similar to that realized in [1]. The flow is from left to right and the subsonic region is on the left side. We work in units where the asymptotic density in the supersonic side, ρ_+ , is equal to 1. The asymptotic values of the Mach numbers for the green (dotted), blue (continuous), and orange (dashed) curves are, respectively, $M_- \approx 0.52, 0.45, 0.4$ and $M_+ = 3.75, 5, 6.25$. The unit of the horizontal axis is $\xi_{+,5}$, the healing length in the supersonic region for the flow with $M_+ = 5$ (blue curves). The plots are shifted so that the sonic horizon $M = 1$ (marked by an horizontal red dashed line the upper right panel) is at $x = 0$. The bottom left plot shows the profile of the adimensionalized gradient $\kappa(x)\xi_{+,5}/c_{+,5}$, where $c_{+,5}$ is the asymptotic downstream sound velocity when $M_+ = 5$. One clearly sees that $\kappa(x)$ identically vanishes on the right of the potential barrier located near $x/\xi_{+,5} = 0.4$. When evaluated at $x = 0$, κ gives the surface gravity κ_H of Eq. (8). The values of $\kappa_H\xi_{+,5}/c_{+,5}$ are 5.5, 5.1, and 4.6. As functions of M_+ , the bottom right plot shows the Hawking temperature $T_H = \kappa_H/2\pi$ adimensionalized by ξ_H/c_H (blue, continuous), ξ_+/c_+ (green, dotted), ξ_-/c_- (orange, dashed), and $\xi_{-,5}/c_{-,5}$ (red, dot-dashed). The first three values increase with M_+ , unlike the last one which is not monotonic.

where $\sigma = \sqrt{\rho_{1,-}^{-1} - \rho_{1,-}^{-2}}$. In the upper plots of Fig. 1 we show the (non-dimensional) density profile and Mach number for three nearby flows. The central blue curve corresponds to $M_+ = 5$. The two others are obtained with relative changes of 25%, i.e., $M_+ = 6.25$ (orange) and 3.75 (green). We shall use these flows to illustrate the typical behavior of the scattering coefficients and their sensitivity to M_+ . It should be also noticed that these flows are stable, and act as attractors in that perturbations propagate outwards from the sonic horizon leaving the solution intact, see Appendix B. Their stability and the smallness of the non-polynomial parameter (discussed in Appendix A) probably explain why the flow observed in Ref. [1] has a profile in good agreement with that of Eq. (7), see Fig. 1b in [1].

In the lower left plot of Fig. 1 we represent the gradient $\kappa(x) = \partial_x(v - c)$ for the following reason. If the analogy with gravity is accurate [3, 4, 7], the spectrum of phonons emitted from the sonic horizon should closely follow the Planck law with an effective temperature given (in units where the Boltzmann and Planck constants are equal to 1) by $T_H = \kappa_H/2\pi$, where $\kappa_H \equiv \kappa(x_H)$ is the analog surface gravity and x_H gives the location of the sonic horizon where $M(x) = 1$. In the waterfall flows, it is given by [9]:

$$\kappa_H = 3\rho_{1,-}^{-5/3} \left(\rho_{1,-}^{1/3} - 1 \right)^{3/2} \left(\rho_{1,-}^{1/3} + 1 \right)^{1/2}. \quad (8)$$

It can be seen in the figure that κ_H is only $\approx 35\%$ of the maximal value of $\kappa(x)$. This is in sharp contrast with the symmetrical flows considered in [7]. It implies that the deviations from the Planck spectrum will be larger than in symmetrical flows with the same κ_H [20]. It should also be noticed that $\kappa_H \approx 5.1 c_{+,5}/\xi_{+,5}$ where $c_{+,5}$ and $\xi_{+,5}$ are the asymptotic downstream sound velocity and healing length for the flow with $M_+ = 5$. By comparison, the

dispersive frequency evaluated at the horizon for the same flow is $c(x_H)/\xi(x_H) \approx 2.9 c_{+,5}/\xi_{+,5}$. Hence $\kappa_H \xi_H/c_H \approx 1.8$. Although it is larger than unity, the expected temperature $T_H = \kappa_H/2\pi$ is only $\approx 0.28 c_H/\xi_H$. Hence, in agreement with [21], we shall see below that the emission spectrum is rather well approximated by the standard relativistic expression. To illustrate the variation of T_H with M_+ in the unit of various dispersive scales, on the lower right plot of Fig. 1, we represent T_H multiplied by ξ_H/c_H , ξ_{+}/c_{+} , ξ_{-}/c_{-} , and $\xi_{-,5}/c_{-,5}$. The first three products go to zero like $(M_+ - 1)^{3/2} / (\sqrt{6}\pi)$ when $M_+ \rightarrow 1$. When $M_+ \rightarrow \infty$, they behave differently: $\xi_H T_H/c_H \sim 3M_+^{1/3}/(2\pi)$, $\xi_{-} T_H/c_{-} \sim 3/(2\pi)$, and $\xi_{+} T_H/c_{+} \sim 3M_+/(2\pi)$. Interestingly, when multiplied by a fixed unit of time, e.g., $c_{-,5}/\xi_{-,5}$, T_H is a non-monotonic function of M_+ . It behaves as $T_H \xi_{-,5}/c_{-,5} \sim \sqrt{2/3}(M_+ - 1)^{3/2}$ for $M_+ \rightarrow 1$ and $T_H \xi_{-,5}/c_{-,5} \sim 3M_+^{-1}$ for $M_+ \rightarrow \infty$.

B. Spontaneous emission of phonons, generalities

To describe the propagation of linear density fluctuations in the above flows, we now adopt a quantum mechanical description [2], following [7] where more details can be found. It is convenient to write the atomic field operator as

$$\hat{\psi}(x, t) = \psi_0(x, t) \left(1 + \hat{\phi}(x, t) \right), \quad (9)$$

where ψ_0 is a known stationary solution of Eq. (2) with mean density $\rho(x)$ and velocity $v(x)$. To first order in $\hat{\phi}$, one obtains the Bogoliubov-de Gennes (BdG) equation, which here reads:

$$i(\partial_t + v(x)\partial_x) \hat{\phi} = -\frac{1}{2\rho(x)} \partial_x \left[\rho(x) \partial_x \hat{\phi} \right] + g\rho(x) \left(\hat{\phi} + \hat{\phi}^\dagger \right). \quad (10)$$

Since the background flow is stationary, we look for stationary solutions of the form

$$\hat{\phi}_\omega(t, x) = e^{-i\omega t} \phi_\omega(x) \hat{a}_\omega + (e^{-i\omega t} \varphi_\omega(x) \hat{a}_\omega)^\dagger. \quad (11)$$

The operators \hat{a}_ω and \hat{a}_ω^\dagger destroy and create a phonon of frequency ω , and obey the usual bosonic commutation relations. This particular form of the decomposition of the field operator follows from the antilinear term in Eq. (10). It can be easily shown that the stationary c-number mode doublet $(\phi_\omega(x), \varphi_\omega(x))$ obeys

$$\begin{aligned} \left((\omega + iv\partial_x) - \frac{1}{2\rho} \partial_x \rho \partial_x - c^2 \right) \phi_\omega &= c^2 \varphi_\omega, \\ - \left((\omega + iv\partial_x) + \frac{1}{2\rho} \partial_x \rho \partial_x + c^2 \right) \varphi_\omega &= c^2 \phi_\omega. \end{aligned} \quad (12)$$

The inner product of two solutions $W_1 = (\phi_1, \varphi_1)$ and $W_2 = (\phi_2, \varphi_2)$ is

$$(W_1 | W_2) \equiv \int_{-\infty}^{+\infty} dx \rho(x) (\phi_1^* \phi_2 - \varphi_1^* \varphi_2). \quad (13)$$

It is conserved in time when considering non-stationary solutions of the time-dependent BdG equation. We call $(W_1 | W_1)$ the norm of the solution represented by the doublet W_1 .

In the asymptotic regions where v and ρ are uniform, any solution of Eq. (12) can be written as a superposition of plane wave doublets $W_{\omega,k}(t, x) = (U_k, V_k) \exp(-i\omega t + ikx)$, where ω and k are related by the dispersion relation

$$\Omega^2 = g\rho k^2 + \frac{k^4}{4}. \quad (14)$$

Here $\Omega \equiv \omega - vk$ is the frequency in the rest frame of the gas. This dispersion relation is represented graphically in Fig. 2. In the following we consider only the case $\omega > 0$. Then, for $\Omega > 0$, U_k and V_k are related by $V_k = D(k, \rho)U_k$, where

$$D(k, \rho) = \frac{\sqrt{g\rho k^2 + k^4/4}}{g\rho} - \left(\frac{k^2}{2g\rho} + 1 \right). \quad (15)$$

When U_k and V_k satisfy the usual relation $|U_k|^2 - |V_k|^2 = 1$, the doublets $W_{\omega,k}$ obey

$$(W_{\omega,k} | W_{\omega',k'}) = 2\pi\rho \delta(k - k'). \quad (16)$$

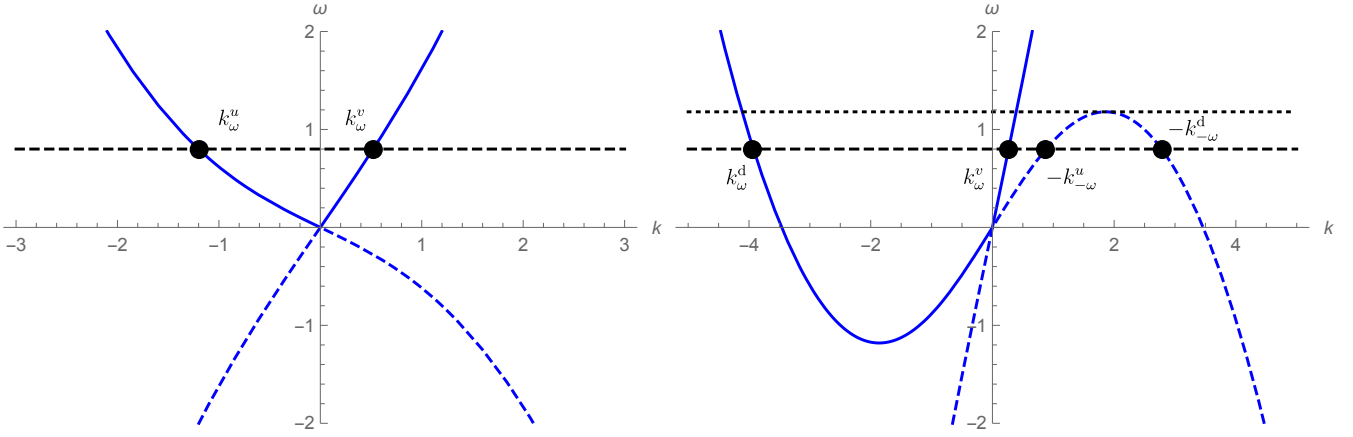


Figure 2. Plot of the dispersion relation in homogeneous subsonic (left) and supersonic (right) flows. The horizontal, dashed, black line corresponds to a fixed frequency. The continuous curves correspond to positive values of $\Omega = \omega - vk$ and the dashed ones to negative values of Ω . One notices that the two extra roots on the right of the right plot have $\Omega < 0$. As explained in the text, they describe phonons carrying a negative energy in the frame where V is stationary. These two extra roots become complex when ω reaches the critical frequency ω_{\max} of Eq. (17), which is here indicated by a dotted line.

For $\Omega < 0$, the solutions of Eq. (12) are doublets $\bar{W}_{\omega,k}$ obtained by exchanging the two components of those with $\Omega > 0$ and taking their complex conjugate. When working with $\omega > 0$, the doublets with $\Omega < 0$ are thus given by $\bar{W}_{-\omega,-k}(t,x) \equiv (V_k^*, U_k^*) \exp(-i\omega t + ikx)$. Importantly, they have a negative norm: $(\bar{W}_{\omega,k}|\bar{W}_{\omega',k'}) = -(\bar{W}_{\omega,k}|W_{\omega',k'})$. The phonons described by $W_{-\omega,-k}$ carry a negative energy equal to $-\omega$ (in units where $\hbar = 1$).

We now study separately subsonic and supersonic flows to identify the number of independent solutions. In a subsonic flow, i.e., $0 < v < c$, there are two real roots in k for $\omega > 0$:

- k_{ω}^u is counter-propagating (its group velocity is negative in the rest frame of the condensate) and left-moving in the frame of $V(x)$;
- k_{ω}^v is co-propagating and right-moving.

The corresponding modes are described by positive norm doublets $W_{\omega,k}$. There are also two complex roots with equal and opposite imaginary parts.

In a supersonic flow parametrized by $M_+ > 1$, there is critical frequency given by [7]

$$\omega_{\max} = \frac{c_+}{\xi_+} \sqrt{M_+ + \sqrt{M_+^2 + 8}} \left(\frac{2(M_+^2 - 1)}{3M_+ + \sqrt{M_+^2 + 8}} \right)^{3/2}. \quad (17)$$

In our unit system, for $M_+ \rightarrow \infty$, one gets $\omega_{\max} \rightarrow 1/2$. When ω crosses ω_{\max} by increasing values, two real roots merge and become complex. For $0 < \omega < \omega_{\max}$, the four roots k_{ω} are real. From left to right in the right panel of Fig. 2, the roots are

- k_{ω}^d is counter-propagating;
- k_{ω}^v is co-propagating and right-moving;
- $-k_{-\omega}^u$ is counter-propagating and right-moving;
- $-k_{-\omega}^d$ is counter-propagating and left-moving.

The superscript “ d ” on the first and last roots indicates that they are dispersive, i.e., that they do not vanish in the limit $\omega \rightarrow 0$. The minus signs in front of the last two roots indicate that the corresponding modes are negative-norm doublets $\bar{W}_{-\omega,-k}(t,x)$ describing negative-energy phonons. These two roots merge when ω reaches ω_{\max} .

When considering transonic stationary flows which interpolate from a sub to supersonic region, these 6 asymptotic modes will be mixed by the scattering on the region where ρ and v depend on x . Then three globally defined and linearly independent doublets are found for $\omega < \omega_{\max}$. To extract the scattering coefficients, two mode bases should

be considered: that made of 3 incoming modes (which each contains asymptotically only one wave with a group velocity oriented towards the horizon) and that made of 3 outgoing modes (which each contains asymptotically only one wave with a group velocity oriented away from the horizon). Following [7], we write the 3×3 scattering as

$$\begin{pmatrix} \phi_\omega^{d,\text{in}} \\ (\varphi_{-\omega}^{d,\text{in}})^* \\ \phi_\omega^{v,\text{in}} \end{pmatrix} = \begin{pmatrix} \alpha_\omega & \beta_{-\omega} & \tilde{A}_\omega \\ \beta_\omega^* & \alpha_{-\omega}^* & \tilde{B}_\omega^* \\ A_\omega & B_\omega & \alpha_\omega^v \end{pmatrix} \begin{pmatrix} \phi_\omega^u \\ (\varphi_{-\omega}^u)^* \\ \phi_\omega^v \end{pmatrix} \quad (18)$$

where the superscripts on the modes have the same meaning as those of the wave-vectors. To avoid any ambiguity, we have completed the superscript of *in*-modes by adding “in”. For the *out*-modes instead the superscript “out” is implicit. In each basis, the 3 globally defined doublets $W_\omega^a(x) = (\phi_\omega^a(x), \varphi_\omega^a(x))$ are orthogonal to each others and have a positive unit norm

$$(W_\omega^a | W_{\omega'}^b) = \delta^{ab} \delta(\omega - \omega'). \quad (19)$$

This normalisation differs from that of Eq. (16) because we here exploit the stationarity of the flow (since the homogeneity is broken near the sonic horizon). Because negative energy phonons are described by doublets of the form $\tilde{W}_{-\omega} = (\varphi_{-\omega}^*, \phi_{-\omega}^*)$ in Eq. (18), the 3×3 matrix is an element of $U(1, 2)$. As a result, for instance, the coefficients of the first line obey

$$|\alpha_\omega|^2 - |\beta_{-\omega}|^2 + |\tilde{A}_\omega|^2 = 1. \quad (20)$$

For more details about these relations, we refer to [14]. The two sets of modes are orthonormal and complete. Using for instance the *out* set, the Fourier component of the field operator with $\omega > 0$ thus reads

$$\hat{\phi}_\omega(x) = \hat{a}_\omega^u \phi_\omega^u(x) + \hat{a}_\omega^v \phi_\omega^v(x) + \hat{a}_{-\omega}^{u\dagger} (\varphi_{-\omega}^u(x))^*. \quad (21)$$

The three operators \hat{a}_ω^u , \hat{a}_ω^v , and $\hat{a}_{-\omega}^u$ destroy respectively an outgoing phonon with wave vector k_ω^u , k_ω^v , and $k_{-\omega}^u$. When starting from the initial vacuum state, the mean numbers of outgoing phonons spontaneously emitted by the scattering on the flow are

$$n_\omega^u = |\beta_\omega|^2, \quad n_\omega^v = |\tilde{B}_\omega|^2. \quad (22)$$

For negative-energy phonons, by energy conservation, we have $n_{-\omega}^u = n_\omega^u + n_\omega^v$.

C. Spectral properties in waterfall background flows

To obtain the scattering coefficients in the three waterfall solutions of Fig. 1, we numerically integrated Eq. (12) following a procedure similar to that of [7], here implemented in *Mathematica* [22]. We first consider the energy spectrum $\epsilon_\omega = \omega |\beta_\omega|^2$ of positive energy *u*-phonons. On the left plot of Fig. 3, for the three flows of Fig. 1, as a function of $\omega/\omega_{\text{max}}$ (where ω_{max} is the corresponding value of the critical frequency of Eq. (17)), we represent $\epsilon_\omega/T_{H,5}$ where $T_{H,5}$ is the Hawking temperature of the central flow with $M_+ = 5$. We see that the three energy spectra are quite similar. We also see that they closely follow the (adimensional) Planck spectrum $\epsilon_\omega^{T_{H,5}}/T_{H,5} = (\omega/T_{H,5})/(\exp(\omega/T_{H,5}) - 1)$ evaluated for the central flow with $M_+ = 5$. In fact, for this flow the maximum value of the difference $|(\epsilon_\omega - \epsilon_\omega^{T_{H,5}})/T_{H,5}|$ is less than 9% for all values of ω .

To study more closely the Planckianity of the spectrum, on the right plot, we represent $T_{\text{eff}}(\omega)/T_H$ for the same flows, where the effective temperature T_{eff} is defined by

$$|\beta_\omega|^2 = \frac{1}{\exp(\omega/T_{\text{eff}}(\omega)) - 1}. \quad (23)$$

In the limit $\omega \rightarrow 0$, for each of the three flows, T_{eff} goes to a value close to the corresponding T_H , with a difference of the order of 10%. Moreover, the slope $dT_{\text{eff}}/d\omega$ evaluated near $\omega = T_H$ is smaller than 0.05. Yet, relative deviations become large when increasing ω (reaching a maximum of $\sim 70\%$). But these occur only for large values of ω/T_H where the energy spectrum is very small. For instance, when T_{eff} differs from T_H by 20%, ϵ_ω/T_H is less than 8%. Although $T_H \xi_H/c_H \approx 1.5$ as discussed above, the values of T_H/ω_{max} for the three flows we consider are 0.062, 0.069, and 0.080. It is the smallness of this ratio which guarantees that the deviations from the Planck spectrum with a temperature $\kappa_H/2\pi$ are, in effect, so small [7, 21].

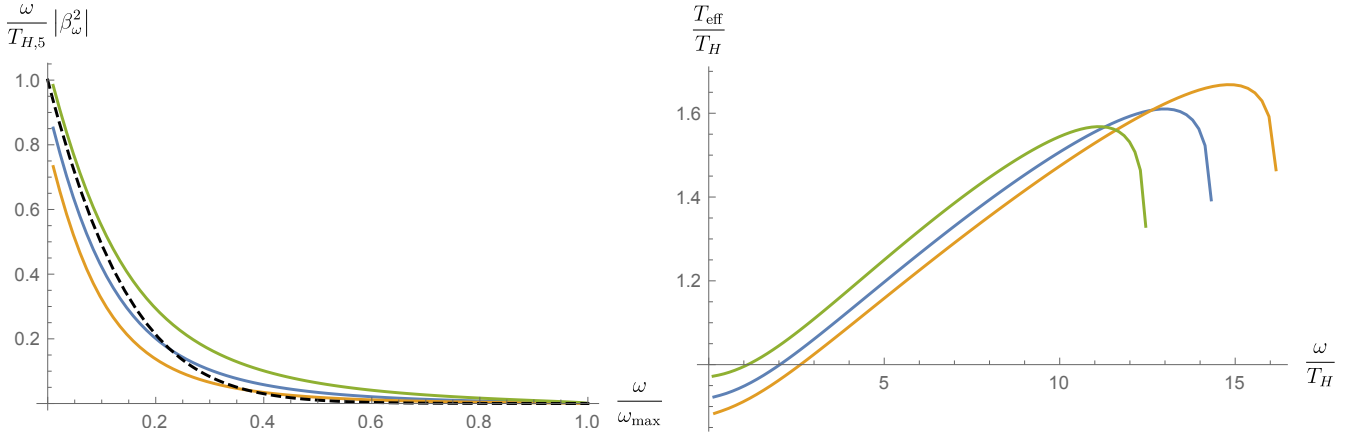


Figure 3. On the left panel, we show the adimensionalized energy spectrum $\epsilon_\omega/T_{H,5}$ of the outgoing phonons spontaneously emitted by the scattering on the sonic horizon of the three flows of Fig. 1, where $T_{H,5} = \kappa_{H,5}/2\pi$ is the Hawking temperature $\kappa/2\pi$ for the flow with the central value of $M_+ = 5$. We use the same conventions, namely green, blue, and orange curves correspond to $M_+ = 3.75, 5, 6.25$. The black dashed line shows the adimensionalized Planck energy spectrum evaluated for this flow. We see that ϵ_ω is slightly larger than the Planck spectrum for $\omega \gtrsim 0.2\omega_{\max} \approx 3T_H$, something which indicates that $T_{\text{eff}}(\omega)$, the effective temperature of Eq. (23), should grow with ω . On the right panel, we show $T_{\text{eff}}(\omega)$ in units of the corresponding value of $T_H(M_+)$ for the same three flows. One clearly sees that $T_{\text{eff}}(\omega)$ becomes significantly larger than T_H , but this occurs in a domain where ϵ_ω is very small. The rapid drop of $T_{\text{eff}}(\omega)$ for large frequency gives approximatively the value of ω_{\max}/T_H for each flow.

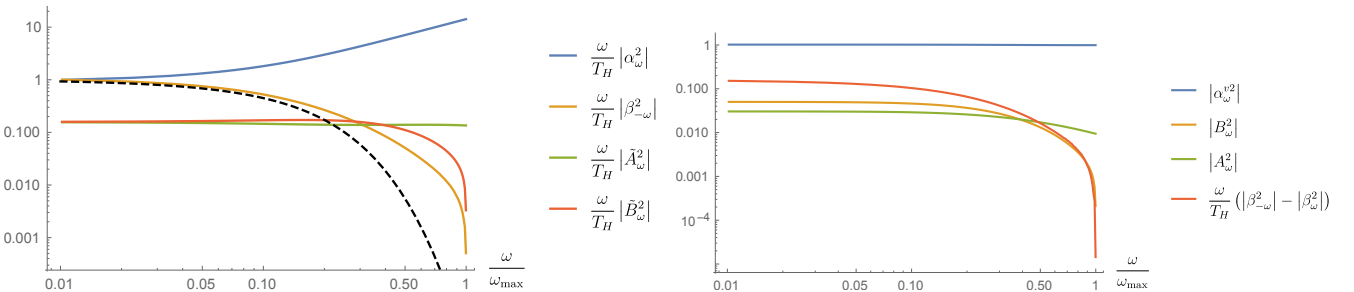


Figure 4. Plots of the squared absolute values of the coefficients of Eq. (18) for the “waterfall” solution with $M_+ = 5$. The left panel shows the coefficients of the first line as well as $|\tilde{B}_\omega^2|$ and the Planck distribution with temperature $T_{H,5}$ (dashed line), all multiplied by $\omega/T_{H,5}$. The right panel shows the coefficients involving the incoming co-propagating v -mode and the difference $(|\beta_{-\omega}^2| - |\beta_\omega^2|)\omega/T_{H,5}$. The smallness of these quantities reveals the weakness of the coupling between the v -mode and the two u -modes.

To pursue the analysis of the scattering, it is instructive to study the other coefficients of Eq. (18). Here we only consider the flow with $M_+ = 5$. It is then appropriate to separate the coefficients whose norm squared diverges like $1/\omega$ for $\omega \rightarrow 0$, from those which remain regular in this limit. (The first ones involve one of the two counter-propagating dispersive incoming waves.) On the left plot of Fig. 4, we show the absolute values of the squared scattering coefficients of the first line of Eq. (18) and that of $|\tilde{B}_\omega^2|$. Besides the Planckianity already discussed, we learn here that for all ω , $|\tilde{A}_\omega^2|$ and $|\tilde{B}_\omega^2|$ both remain approximately 6 times smaller than $|\alpha_\omega^2|$. The co-propagating v -mode is thus relatively weakly coupled to the two u -modes. This is confirmed by the right plot of Fig. 4, where we show the absolute values of the squared coefficients of the third line involving the v -mode. We see that $|A_\omega^2|$ and $|B_\omega^2|$ are smaller than 0.06 for all values of ω . The weakness of the coupling of the v -mode also explains why $|\beta_{-\omega}|$ remains close to $|\beta_\omega|$, as can be seen by the red curve in the right panel. Indeed, the difference $|\beta_{-\omega}^2| - |\beta_\omega^2|$ can be shown to be equal to $|\tilde{B}_\omega^2|$ for $\omega \ll T_H$ [7].

To complete the analysis, we study in Fig. 5 two key properties characterizing the spectrum for the entire series of

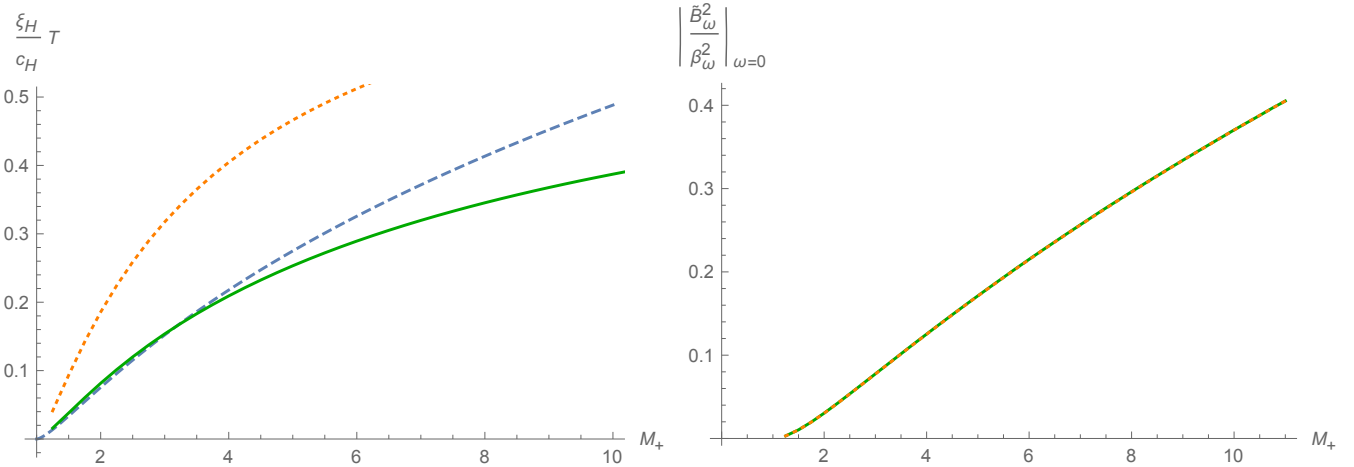


Figure 5. Left panel: As functions of the supersonic Mach number M_+ , we show the limit $\omega \rightarrow 0$ of T_{eff} of Eq. (23) (green, continuous), the Hawking temperature T_H (blue, dashed), and T_{step} obtained with the density profile of Eq. (24) (orange, dotted), all adimensionalized by multiplication by the dispersive time-scale ξ_H/c_H . Right panel: Ratio of $|\tilde{B}_\omega^2 / \beta_\omega^2|_{\omega=0}$ for the waterfall (green, continuous) and for the “step-like” (orange, dotted) profiles. The very close agreement indicate that, for $\omega \rightarrow 0$, the ratio $|\tilde{B}_\omega^2 / \beta_\omega^2|$ only depends on the asymptotic values of v and c .

waterfall solutions. On the left plot, as functions of M_+ , we represent the low frequency effective temperature T_{eff} and T_H , both adimensionalized by c_H/ξ_H . For all values of M_+ , we see that T_{eff}/T_H remains in the interval $[0.75, 1.25]$, thereby indicating that the low-frequency effective temperature is always well approximated by $T_H = \kappa_H/2\pi$.

To estimate the largest value of the effective temperature one can obtain for a monotonic flow given the asymptotic values of v and c on both sides, we also represent another low frequency effective temperature, T_{step} , for a monotonic flow characterized by the density ²

$$\rho_{\text{step}}(x) = \frac{1 + \rho_{1,-}}{2} + \frac{1 - \rho_{1,-}}{2} \tanh\left(\frac{x}{\sigma}\right). \quad (24)$$

In our simulations, we took $\sigma = \xi_-/8$ (decreasing σ does not significantly modify the results we present.) For all values of M_+ , we observe that T_{step} is larger than T_{eff} by a factor close to 2. It should be noticed that the temperature observed in [1] is $(T_{\text{eff}}\xi_-/c_-)^{\text{obs}} \approx 0.4$, which is larger than both $T_{\text{eff}}\xi_-/c_- \approx 0.15$ and $T_{\text{step}}\xi_-/c_- \approx 0.29$. We currently have no explanation for this excess. It could be related to the fact that the observed flow cannot be accurately described by a one-dimensional flow, see footnote 1, although the analysis of Appendix A 2 seems to indicate that the corrections associated with the improved description are to small to explain the excess.

On the right plot, as functions of M_+ , we represent the zero-frequency limit of the ratio $|\tilde{B}_\omega^2| / |\beta_\omega^2|$ for the waterfall solution and the step-like profile of Eq. (24). This quantity characterizes the relative importance of the $u - v$ pair creation channel with respect to the standard one involving the two u -modes. Since $|\tilde{B}_\omega^2|$ and $|\beta_\omega^2|$ both diverge as $1/\omega$ for $\omega \rightarrow 0$, their ratio is a constant at low frequency. We observe that it is roughly linear in $M_+ - 1$ and becomes important for large values of M_+ . We also observe that it only depends on the asymptotic values of v and c .

In brief, for the flows here considered and when working in the initial vacuum state, n_ω^u , the mean occupation number of outgoing positive frequency phonons, closely follows the relativistic expression in the relevant frequency domain $\omega/T_H \lesssim 1$, both in the Planckian character of the spectrum and in the value of the effective temperature. The spectrum of negative energy phonons, $n_{-\omega}^u$, which includes the spontaneous production of $u - v$ pairs of phonons, is larger than n_ω^u by $\approx 15\%$ at low frequency when $M_+ = 5$.

² Notice that the expressions in the appendix B of [21] for the spectrum in the sharp profile limit should be generalized as Eq. (B13) of that reference requires that $\log(v(x)/v_H)$ be symmetric with respect to x_H in the step-like limit, while the waterfall solutions become very asymmetric for $M_+ \gg 1$.

III. THE TWO-POINT CORRELATION FUNCTION

A. Generalities

Following Refs. [10, 11], J. Steinhauer measured the density-density correlation function at a given time after the formation of the horizon. Explicitly, he studied the adimensional 2-point function [1]

$$G_2(x, x') = \sqrt{\frac{\xi_{\text{sgn}(x)} \xi_{\text{sgn}(x')}}{\rho_{\text{sgn}(x)} \rho_{\text{sgn}(x')}}} \langle \delta \rho(x) \delta \rho(x') \rangle, \quad (25)$$

where $x = 0$ is the location of the sonic horizon $M = 1$. Neglecting the residual time dependence associated with its formation, and assuming that the background flow is stationary, it is appropriate to work at fixed ω and write the correlation function as an integral over ω : $G_2(x, x') = \int_{-\infty}^{\infty} d\omega G_\omega(x, x')$, see Secs. IV.D and IV.F of [7]. We briefly review the main points of that analysis.

When considering density fluctuations, since Eq. (9) gives $\delta \hat{\rho}(t, x)/\rho(x) = \hat{\phi}(t, x) + \hat{\phi}(t, x)^\dagger$, it is appropriate to introduce the modes $\chi_\omega^a = \phi_\omega^a + \varphi_\omega^a$, as χ_ω^a is the only combination which enters $G_\omega(x, x')$. We now assume that the temperature is sufficiently low that the initial state is well approximated by the vacuum, as seems to be the case in the experiment of [1]. In this case, for $\omega > 0$, $x' > 0$, and $x < 0$, $G_\omega(x, x')$ reads

$$G_\omega^{\text{vac}}(x, x') = \sqrt{\frac{\xi_+ \xi_-}{\rho_+ \rho_-}} \rho(x) \rho(x') \left(\chi_{-\omega}^{\text{in}, u}(x) \right)^* \chi_{-\omega}^{\text{in}, v}(x'). \quad (26)$$

This expression can be straightforwardly generalized to account for initial states which are incoherent, i.e., fully described by the mean occupation numbers $\bar{n}_\omega^{\text{in}, u}$, $\bar{n}_\omega^{\text{in}, v}$, and $\bar{n}_{-\omega}^{\text{in}, u}$ of the three types of incoming phonons.

When $x < 0$ and $x' > 0$ are taken sufficiently far away from the horizon in the sub and supersonic homogeneous regions, the in-modes $\chi_{-\omega}^{\text{in}, u}$ are superpositions of 4 asymptotic modes $\chi_\omega^{\text{a, as}}$: the outgoing mode $\chi_\omega^{\text{u, as}}$ on the sub sonic side, and three modes in the supersonic side (the incoming, and two outgoing). When the initial state is incoherent, only the three outgoing modes interfere constructively when integrating over ω to obtain $G_2(x, x')$.³ Explicitly they are given by

$$\begin{aligned} \chi_\omega^{\text{u, as}}(x < 0) &= S_-^u(\omega) e^{ik_\omega^u x}, \\ \chi_{-\omega}^{\text{u, as}}(x' > 0) &= S_+^u(-\omega) e^{ik_{-\omega}^u x'}, \\ \chi_\omega^{\text{v, as}}(x' > 0) &= S_+^v(\omega) e^{ik_\omega^v x'}. \end{aligned} \quad (27)$$

In these expressions, $S_\pm^a(\omega)$ is the structure factor of the corresponding outgoing mode evaluated on the right (+) or left (-) asymptotic side. With our normalization conventions, they are given by

$$S_\pm^a(\omega) = \frac{u_{k_\omega^a, \pm} + v_{k_\omega^a, \pm}}{\sqrt{2\pi \rho_\pm}} \left| \frac{dk_\omega^a, \pm}{d\omega} \right|^{1/2}, \quad (28)$$

where u_k and v_k are the usual coefficients obeying $|u_k|^2 - |v_k|^2 = 1$ and $v_k = D_k u_k$, see Eq. (15). It should be noticed that the three outgoing modes are hydrodynamical. This means that the correlation pattern will be a low wavenumber one, unlike what is found when considering white hole flows [24].

Keeping only the above outgoing modes, for $\omega > 0$, one obtains:

$$\frac{1}{\sqrt{\xi_+ \xi_- \rho_+ \rho_-}} G_\omega^{\text{vac}}(x, x') = e^{ik_\omega^u x} \times \left(\mathbb{A}_\omega e^{-ik_\omega^v x'} + \mathbb{B}_\omega e^{ik_{-\omega}^u x'} \right). \quad (29)$$

(Including the prefactor of the left-hand side in the coefficients $\mathbb{A}_\omega, \mathbb{B}_\omega$ would multiply their norm by $\sqrt{\xi_+ \xi_- \rho_+ \rho_-} \approx 7.5$ for the flow with $M_+ = 5$.) In the incoming vacuum, one finds that the two complex amplitudes can be written as [7]

$$\begin{aligned} \mathbb{A}_\omega &= S_-^u(\omega) S_+^v(\omega) \beta_\omega^* \tilde{B}_\omega, \\ \mathbb{B}_\omega &= S_-^u(\omega) S_+^u(-\omega) \beta_\omega^* \alpha_{-\omega}. \end{aligned} \quad (30)$$

The first accounts for the correlations between v phonons and negative energy partners, while the second accounts for correlations between u -phonons.

³ It should be noticed that this is not the case when working in momentum space with $G_2(k, k')$. Indeed, in that case, the incoming mode constructively interferes with both outgoing modes, as was observed in [23].

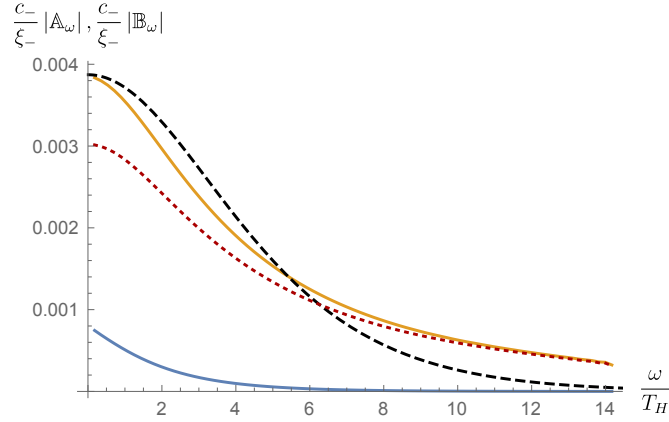


Figure 6. We represent the absolute value of the spontaneous correlation terms A_ω (blue) and B_ω (orange) defined in Eq. (30) calculated for the waterfall solution with $M_+ = 5$, and adimensionalized by the dispersive frequency c_-/ξ_- . The dotted line shows $|B_\omega|$ when the initial state of the co-propagating v -modes is a thermal state with an initial temperature $T_{\text{in}} = 10T_H$. The black, dashed curve shows the relativistic limit for B_ω given in Eq. (31).

B. Strength of correlations and their relativistic pattern

As can be seen in Fig. 6, for the flow with $M_+ = 5$, $|A_\omega|$ is smaller than $|B_\omega|$ by a factor ≈ 5 . It should be noticed that the ratio $|A_\omega| / |B_\omega|$ significantly varies with M_+ . For instance, for the three flows of Fig. 1, its limit $\omega \rightarrow 0$ is close to 0.13 for $M_+ = 3.75$, 0.19 for $M_+ = 5$, and 0.24 for $M_+ = 6.25$. (This dependence is corroborated by the curves shown on the right plot of Fig. 5.)

It should be also noticed that $|B_\omega|$ closely follows the corresponding relativistic expression,

$$B_\omega^{\text{relat.}} = \frac{e^{\omega/(2T_H)}}{e^{\omega/T_H} - 1} e^{i \arg(\alpha_{-\omega}^{\text{relat.}} / \beta_\omega^{\text{relat.}})} \frac{\omega \sqrt{\xi_+ \xi_-}}{4\pi \sqrt{\rho_+ \rho_-} |v_+ - c_+| |v_- - c_-|}, \quad (31)$$

which is indicated by a dashed line. When neglecting the coupling between the v -mode and the two u -modes, the first factor comes from the fact that $|\beta_\omega^{\text{relat.}}|^2$ follows the Planck law with temperature $T_H = \kappa_H/2\pi$. The phase plays no role here and shall be studied below. The normalisation comes from taking the dispersionless limit ($\xi_\pm \rightarrow 0$) of the structure factors of Eq. (28).

In preparation for the subsequent analysis, in Fig. 6 we have also represented by a dotted line the strength of the correlations when the initial state of the co-propagating incoming v -modes is a thermal state with temperature $T_{\text{in}} = 10T_H$ in the fluid frame. (To get this result, we used the complete expression of the uu -correlation which includes the stimulated processes [7].) We see that increasing significantly the initial temperature of v -modes only slightly decreases B_ω for low frequencies. We also see that the strength of correlations remains largest at low frequency.

Having shown that the vacuum relativistic expressions give reliable approximations at fixed ω , it is instructive to integrate them over ω to get the relativistic version of the equal-time correlation function of Eq. (25). When x and x' are not too close to the horizon ($|x|, |x'| \gg \xi_+, \xi_-$), the relativistic limit of Eq. (25) gives two types of expressions. When $xx' < 0$ with $x < 0$, one gets [10]:

$$G_2^{\text{rel}}(x, x') \approx \frac{-\pi T_H^2 \xi_+ \xi_-}{4 |v_+ - c_+| |v_- - c_-| \cosh^2(\pi T_H (u_L(x) - u_R(x')))}, \quad (32)$$

where $u_{R/L}(x)$ give the values of the null characteristic on each side of the horizon. When $xx' > 0$, say on the subsonic side $x < 0$ one gets [25]

$$G_2^{\text{rel}}(x, x') \approx \frac{\pi T_H^2 \xi_-^2}{4 (c_- - v_-)^2 \sinh^2(\pi T_H (u_L(x) - u_L(x')))}. \quad (33)$$

A similar expression applies on the supersonic (+) side. On the left panel of Fig. 7, we represent G_2^{rel} in the (x, x') plane for the waterfall solution with $M_+ = 5$. The oblique white bands correspond to values outside the range represented in colors. (From Eq. (33), G_2 diverges in the coincidence point limit $x \rightarrow x'$.)

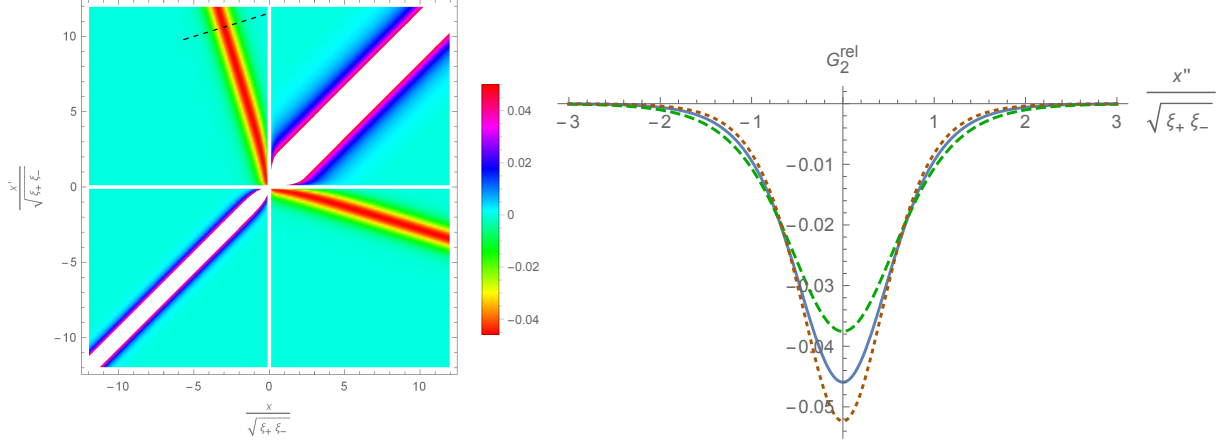


Figure 7. Left: We show $G_2^{\text{rel}}(x, x')$ as a function of x and x' , given by Eq. (C7) with a varying normalization factor to match Eq. (25). The dashed segment represents the domain represented on the right panel. Right: We show $G_2^{\text{rel}}(x, x')$ of Eq. (32) for $x \ll -\xi_-$ and $x' \gg \xi_+$, evaluated along a line orthogonal to the locus of its minima. x'' is a coordinate along this line, defined by $x'' = 0$ when G_2 reaches its minimum and $|dx''| = \sqrt{dx^2 + dx'^2}$. The three curves correspond to $M_+ = 3.75$ (green, dashed), 5 (blue, continuous), and 6.25 (orange, dotted).

In the right panel we show $G_2^{\text{rel}}(x, x')$ evaluated along a segment orthogonal to the locus of the minima in the asymptotic region $x \ll -\xi_-$, $x' \gg \xi_+$. It is represented schematically by a dashed segment on the left panel. The width of the hollow is about twice as large as that reported in [1]. It is also interesting to study the angle between the horizontal and the line of maxima of the correlations in the domain $x < 0, x' > 0$. It is given by

$$\begin{aligned} \theta &= \pi + \arctan((c_+ - v_+)/(c_- - v_-)) \\ &= \pi - \arctan(M_+ + M_+^{1/2}), \end{aligned} \quad (34)$$

For the three values of M_+ we used (3.75, 5, 6.25), this gives 1.85rad, 1.87rad, and 1.90rad. The value reported in [1] ($\theta^{\text{obs}} \approx 2.2\text{rad}$) is slightly larger than the maximal value of Eq. (34) accessible with waterfall solutions, which is $\approx 2.03\text{rad}$.

C. Non-separability

As discussed in [13–16], the strength of the correlations $|\mathbb{B}_\omega|$ determines the non-separability of the state. More precisely, whenever the difference \mathbb{D}_ω , defined by

$$\mathbb{D}_\omega \equiv |\mathbb{B}_\omega^2| - n_\omega^u n_{-\omega}^u (S_+^u(\omega) S_-^u(-\omega))^2, \quad (35)$$

is positive, the bi-partite state of the u -phonons of frequency $\pm\omega$ is non-separable. When the initial state is vacuum, \mathbb{D}_ω can be shown to be positive definite. Yet it is of value to study its behavior as a function of ω . On the left panel of Fig. 8, it is represented by a continuous line. By a dashed line we present its relativistic limit

$$\mathbb{D}_\omega^{\text{relat.}} = \left(\frac{\omega \sqrt{\xi_+ \xi_- / \rho_+ \rho_-}}{4\pi |v_+ - c_+| |v_- - c_-|} \right)^2 \frac{1}{e^{\omega/T_H} - 1}. \quad (36)$$

We clearly see that the two curves closely agree, as can be understood from the near Planckianity of the spectrum and the weakness of the coupling to the co-propagating v -mode (which affects the difference $n_\omega^u - n_{-\omega}^u$).

It should be also pointed out that \mathbb{D}_ω and $\mathbb{D}_\omega^{\text{relat.}}$ are bounded from above, see [14, 26, 27]. When working in the initial vacuum, a Cauchy-Schwarz inequality implies that \mathbb{D}_ω is smaller than (see Eq. B4 in [27])

$$\mathbb{D}_\omega^{\text{max}} \equiv |\beta_{-\omega}|^2 (S_+^u(\omega) S_-^u(-\omega))^2. \quad (37)$$

This maximal value is represented by a dotted line on the left panel of Fig. 8. Interestingly it reaches a non-zero value when $\omega \rightarrow \omega_{\text{max}}^-$. This is due to the fact that the structure factor $S_-^u(-\omega)$ diverges as $(\omega - \omega_{\text{max}})^{-1/4}$ in this

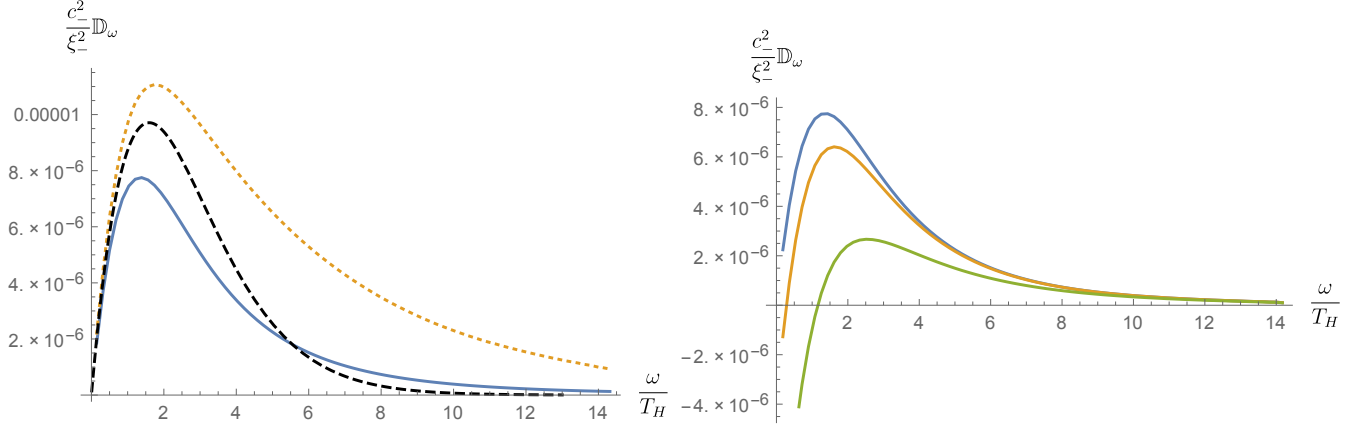


Figure 8. Plot of the quantity \mathbb{D}_ω of Eq. (35) computed for the waterfall solution with $M_+ = 5$, and adimensionalized by the squared frequency $(c_-/\xi_-)^2$. On the left panel, the blue continuous line gives the numerical value predicted by the Bogoliubov-de Gennes equation, while the black, dashed line shows its relativistic limit of Eq. (36). The dotted orange line shows the maximum value of \mathbb{D}_ω of Eq. (37). On the right panel, we show how \mathbb{D}_ω varies when assuming that the co-propagating incoming v -modes have an initial temperature T_{in} . Curves are shown for $T_{\text{in}}/T_H = 10^{-6}$ (blue), 3 (orange), and 10 (green).

limit. Working with relativistic settings in the initial vacuum, the situation is simpler because $\mathbb{D}_\omega^{\text{relat.}}$ of Eq. (36), the dashed curve, already gives the maximal value. This is due to the fact that the coupling to the co-propagating v -mode identically vanishes in these settings.

To test the dependence of non-separability with respect to the initial state of the phonons, we assume the initial state is thermal in the laboratory frame, i.e., in the frame of the condensed fluid in the subsonic region. To compute the initial mean occupation numbers of the counter-propagating dispersive u -modes in the supersonic region requires in principle the knowledge of the whole time-dependence and the fall-off of the condensate density for $x \rightarrow +\infty$. Irrespective of these details, one finds that modes with frequencies $\omega \approx 0$ in the black-hole frame correspond to large frequencies $\Omega^u \approx |v_H k_\omega^d|$ in the laboratory frame. For dispersive modes, $|v_H k_\omega^d|$ is of the order of ω_{max} , and thus much larger than T_H . As a result, their initial population will be suppressed. In a first approximation, one can thus neglect their contribution and consider only the initial occupation number of incoming v -modes

$$\bar{n}_\omega^{v,\text{in}} = \left(e^{\Omega^v / T_{\text{in}}} - 1 \right)^{-1}, \quad (38)$$

where $\Omega^v = \omega - v_- k_\omega^v$. The right panel of Fig. 8 shows \mathbb{D}_ω for $T_{\text{in}}/T_H = 10^{-6}$, 3, and 10. As was found in [13–15], the temperature has the tendency to reduce the non-separability of the state, with low-frequency modes becoming separable before high-frequency ones. Overall, the non-separability is strongly reduced only when T_{in} becomes of the order of $10T_H$. This is another consequence of the weakness of the couplings involving the co-propagating v -mode.

D. Phase of uu correlations

In the previous subsection we studied the strength of the correlations which is governed by the absolute value of \mathbb{B}_ω . Here we consider the phase $\arg \mathbb{B}_\omega$, which is equal to $\arg(\alpha_{-\omega} \beta_\omega^*)$. It does not depend on the arbitrary phase of the (globally defined) incoming modes, but it does depend on the phase of the asymptotic outgoing modes of wave number $k_{\pm\omega}^u$. Each of them is asymptotically given by $k_{\pm\omega}^u(x - x_H) + C_{\pm\omega}$, where $C_{\pm\omega}$ are two real constants. In this paper, we work with $C_{\pm\omega} = 0$, see Eq. (28). (In the body of the paper we fix the origin of x so that $x_H = 0$.)

We now consider the trajectories in the $x - x'$ plane where the equal-time correlations among u -phonons reach their maximal intensity, see Fig. 7 for their relativistic counterpart. To get the locus of constructive interferences at a given time, one should impose that the phase of the \mathbb{B}_ω term of Eq. (29) is stationary, i.e., [7]

$$(\partial_\omega k_\omega^u)x + (\partial_\omega k_{-\omega}^u)x' = -\partial_\omega \arg(\alpha_{-\omega} \beta_\omega^*). \quad (39)$$

We thus see that $\partial_\omega \arg(\alpha_{-\omega} \beta_\omega^*)$ introduces a non-trivial shift. To our knowledge it has not been studied before in

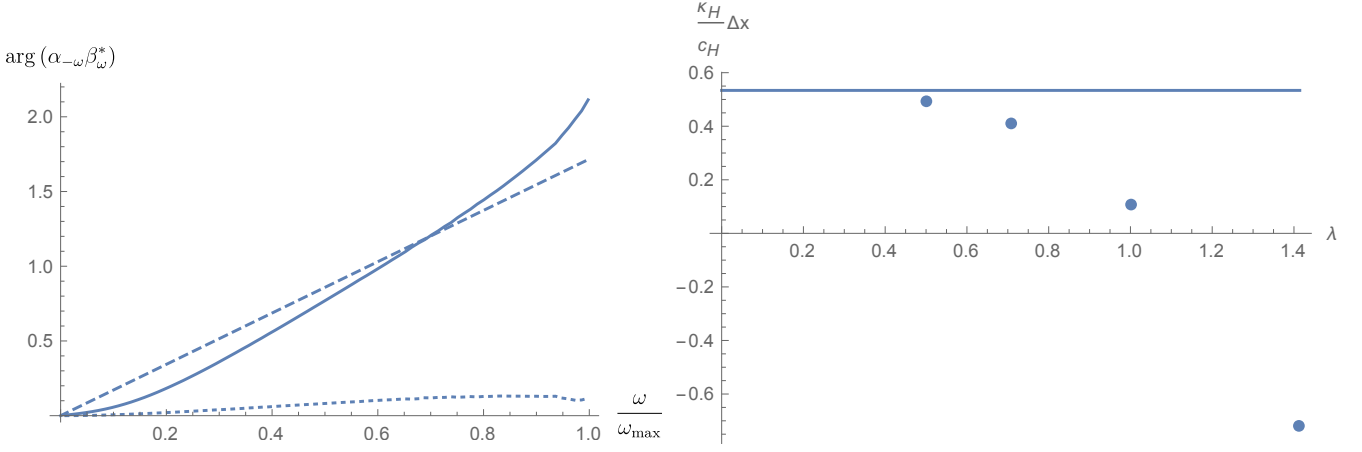


Figure 9. Left: As a function of ω/ω_{\max} , we show the phase of $\alpha_{\omega}\beta_{-\omega}^*$ for the flow of Fig. 1 with $M_+ = 5$. The dashed line shows the relativistic phase which is obtained from Eq. (C14). The dotted line shows $\arg(\alpha_{-\omega}\beta_{\omega}^*) - \arg(\alpha_{\omega}\beta_{-\omega}^*)$. Its smallness is another test of the validity of the relativistic approximation, which predicts that this difference should vanish. Right: As a function of λ of Eq. (41), we show the shift $x_M(\omega = 0) - x_H$, see Eq. (40), evaluated in the small-frequency limit and adimensionalized by the surface gravity length c_H/κ_H . The horizontal line shows the relativistic result of Eq. (C11).

the present context, although its existence was mentioned in [7].⁴ When $\partial_{\omega} \arg(\alpha_{-\omega}\beta_{\omega}^*) \neq 0$, the asymptotic straight line $x(x')$ solution of Eq. (39) will not cross exactly the sonic horizon at $x_H = 0$ when $x' = 0$. Rather x will be equal to x' at the point x_M given by

$$x_M(\omega) = -\frac{\partial_{\omega} \arg(\alpha_{-\omega}\beta_{\omega}^*)}{\partial_{\omega} k_{\omega}^u + \partial_{\omega} k_{-\omega}^u}, \quad (40)$$

where the denominator is evaluated in the asymptotic regions.

In the left panel of Fig. 9, the continuous line shows $\arg(\alpha_{-\omega}\beta_{\omega}^*)$ as a function of ω/ω_{\max} for the flow of Fig. 1 with $M_+ = 5$. As can be seen, its slope is nearly constant except for $\omega \approx \omega_{\max}$ and $\omega \approx 0$. In the intermediate frequency domain, the shift $x_M(\omega)$ will be thus nearly independent of ω . The dashed line shows $\arg(\alpha_{-\omega}\beta_{\omega}^*)$ for the relativistic field propagating in the same background flow. Its value is computed in Appendix C. Quite surprisingly, its slope does not vanish and agrees rather well with the slope of Fig. 9 in the intermediate frequency domain. It is therefore interesting to study the relativistic limit to see the residual role played by short distance dispersion. To this end, we numerically computed the low frequency slope when decreasing the healing length. Specifically, we solved the rescaled BdG equations

$$\begin{aligned} \left((\omega + iv\partial_x) - \frac{\lambda^2}{2\rho} \partial_x \rho \partial_x - \frac{c^2}{\lambda^2} \right) \phi_{\omega} &= \frac{c^2}{\lambda^2} \varphi_{\omega}, \\ - \left((\omega + iv\partial_x) + \frac{\lambda^2}{2\rho} \partial_x \rho \partial_x + \frac{c^2}{\lambda^2} \right) \varphi_{\omega} &= \frac{c^2}{\lambda^2} \phi_{\omega}, \end{aligned} \quad (41)$$

for several values of λ . This rescaling neither modifies the background flow nor the conserved scalar product, but multiplies the dispersive length scale by λ . The relativistic limit thus corresponds to $\lambda \rightarrow 0$, while Eq. (12) is recovered when $\lambda = 1$. Numerical results are shown in Fig. 9, right panel. Although we were not able to obtain trustworthy values of Δx for $\lambda < 1/2$, the figure indicates that Δx converges to the value obtained from Eq. (C11) when decreasing λ towards 0. We hope that the shift $x_M - x_H$ could be measured in forthcoming experiments.

IV. CONCLUSION

In Section II, we first analyzed the stationary, asymptotically homogeneous transonic background flows which are solutions of the one-dimensional GPE in a step-like potential. These are described by a one-parameter family of

⁴ A phase similar to $\arg(\alpha_{\omega}\beta_{-\omega}^*)$ governs the locii of the nodes of the stationary zero-frequency modulation emitted in transonic flows which are analogous to white holes. [28, 29]. When working in homogeneous time dependent settings, such as in inflationary cosmology [26] and in condensed matter [30, 31], a similar phase, also given by the argument of the product $\alpha\beta^*$ of two Bogoliubov coefficients, fixes the location of the nodes of the equal time correlations.

stable waterfall solutions. When M_+ , the Mach number in the asymptotic supersonic region, is significantly larger than 1, they have high spatial gradients near the sonic horizon where $M = 1$. Indeed, for $M_+ \gtrsim 3$, the surface gravity κ_H is larger than the dispersive scale measured on the horizon. These flows are highly asymmetrical with respect to the horizon: for large M_+ , the gradients of flow parameters (such as the sound speed c or the velocity v) increase significantly on the supersonic side. As a by-product of the strong asymmetry, when $M_+ \gtrsim 3$, the surface gravity (measured on the horizon) decreases when increasing M_+ . These results are summarized in Fig. 1.

We then studied the spectrum of the phonons spontaneously emitted when the initial state is vacuum. In spite of the fact that the surface gravity κ_H is larger than the dispersive scale, for $M_+ \lesssim 6$, we found that the emission spectrum is well approximated by its relativistic prediction, namely a Planck spectrum governed by the temperature $T_H = \kappa_H/2\pi$. This can be understood from the fact that the critical frequency ω_{\max} above which the emission spectrum vanishes is about 15 times larger than T_H for $M_+ = 5$. We also found that the spontaneous production of phonons involving a co-propagating mode (which is not related to the standard Hawking effect) is subdominant. We finally studied the behavior of T_{step} , the low frequency temperature computed in step-like flows which possess the same asymptotic properties as the waterfall solutions. We expect that T_{step} gives a reliable estimate of the maximal temperature in flows with a monotonic $\rho(x)$ and we found that it is about twice the temperature in waterfall flows. When compared to the experimental data of [1], the observed temperature is about 30% higher than T_{step} . This could be explained by the difference between one-dimensional waterfall solutions and the experimentally realized flow.

In Section III, we studied the strength and phases of the correlations between phonons emitted on either side of the sonic horizon. In agreement with the above study of spectral properties, we found that the frequency dependence of the strength of the correlations is well approximated by its relativistic expression. We showed that, because of the smallness of the coupling terms involving co-propagating mode, the correlation spectrum is hardly affected when attributing an initial temperature to these phonons. We then studied the pattern of equal-time correlations, and we showed that their profile has a very narrow width, of the order of the healing length evaluated at the horizon. This is a consequence of the above noticed fact that the surface gravity κ_H is larger than the dispersive scale measured on the horizon. We also showed that this width hardly varies for M_+ from 3.75 to 6.25 and is about twice the value reported in [1]. At present, together with the intensity of the correlations, this is the largest discrepancy between the observed properties and the predictions one can theoretically draw. We hope that the present analysis could help sorting out this problem, and be used in forthcoming experimental works.

We also studied the phase of the product of scattering coefficients which enters in the long distance correlation pattern. We found that there is a non trivial, almost linear, dependence in ω which induces a finite shift of the location of the equal-time correlations in the (x, x') plane. We also showed that this shift persists when taking the relativistic limit. In Appendix C we computed its value for various background flows, including in waterfall flows. We showed that it is a significant fraction of the typical horizon length c_H/κ_H . We hope it could be measured in forthcoming experiments. In Appendix D we briefly studied the frequency dependence of individual scattering coefficients. Although it is unclear whether they could be measured when working in vacuo or in thermal states, they can be measured in the stimulated regime by sending towards the horizon a coherent wave of phonons, as is done in analog gravity experiments based on water waves in flumes.

ACKNOWLEDGMENTS

We thank Jeff Steinhauer for many interesting discussions which motivated this work. This work was supported by the French National Research Agency by the Grants No. ANR-11-IDEX-0003-02 and ANR-15-CE30-0017-04 associated respectively with the projects QEAGE (Quantum Effects in Analogue Gravity Experiments) and HARALAB (Hawking Radiation in the Laboratory).

Appendix A: Non-polynomial Schrödinger equation

In this appendix we show how the waterfall solutions and the spectrum of phonons are modified when using the non-polynomial Schrödinger equation (NPSE) [32] coming from integration of the 3-dimensional GPE over two directions in a harmonic trap. To this end, we compute the background flow and scattering coefficients from the NPSE, which are then compared with the results of the main text. Before doing the explicit calculation, it is useful to keep in mind the expected order of magnitude of the deviations. The one-dimensional GPE corresponds to the leading order in an expansion of the NPSE in the non-dimensional parameter $a_s \rho$, where a_s is the scattering length of the atoms and ρ their one-dimensional number density. In the experiment of [1], the condensate is made of ^{87}Rb atoms with $a_s \approx 5 \times 10^{-9} \text{ m}$. On the other hand, the maximum value of ρ reported in [1] in the region used for analysing the data is close to $2 \times 10^7 \text{ m}^{-1}$. The maximum value of $a_s \rho$ is thus close to 0.1, indicating that the GPE should be a relatively

good approximation although corrections from the next orders in $a_s \rho$ should be visible. This is explicitly shown in the following subsections. We first explain how, in non-dimensional units, the knowledge of the two asymptotic densities and of the Mach number on one side fully determines the waterfall solution. We then compute the effective temperature and relative phase of the coefficients α_ω and β_ω , and we compare them with results of the GPE.

1. Waterfall solutions

The NPSE may be written as [32, 33]

$$i\hbar\partial_t f = \left(-\frac{\hbar^2}{2m}\partial_x^2 + V(x) + \frac{gN}{2\pi a_\perp^2} \frac{|f^2|}{\eta} \right) f + \frac{\hbar\omega_\perp}{2} \left(\eta + \frac{1}{\eta} \right) f, \quad (\text{A1})$$

where $\eta \equiv \sqrt{1 + 2a_s N |f^2|}$. In this expression, f is the longitudinal part of the condensate wave function, N the number of atoms, a_s the scattering length, ω_\perp the transverse frequency of the trap (assumed to take the same value in the two transverse directions), and $a_\perp \equiv \sqrt{\hbar/(m\omega_\perp)}$. Notice that there are two additional scales with respect to the GPE: a time scale ω_\perp^{-1} and a length scale a_s . As we show below, the waterfall solution is thus described by three quantities instead of one in the case studied in the main text. To reduce the number of parameters, it is useful to work with the non-dimensional quantities $\psi \equiv \sqrt{2N a_s} f$, $\bar{t} \equiv \omega_\perp t$, $\bar{x} \equiv x/a_\perp$, $\bar{V} \equiv V/(\hbar\omega_\perp)$, and $\bar{g} \equiv g/(4\pi\hbar\omega_\perp a_\perp^2 a_s)$. Since we will work only with these non-dimensional quantities, we shall remove the bars in the following. The NPSE then becomes

$$i\partial_t \psi = \left(-\frac{1}{2}\partial_x^2 + V(x) + \frac{1}{2} \left(\eta + \frac{1}{\eta} \right) + g \frac{|\psi^2|}{\eta} \right) \psi, \quad (\text{A2})$$

where $\eta = \sqrt{1 + |\psi^2|}$. As in the main text, we assume $g > 0$.

We look for stationary solutions of the form

$$\psi(x, t) = e^{-i\omega t} \sqrt{\rho(x)} e^{i \int^x u(y) dy}, \quad (\text{A3})$$

where ρ and u are two real functions, and $\omega \in \mathbb{R}$. Taking the imaginary part of Eq. (A2) gives $J \equiv \rho u = Cst$. The real part of Eq. (A2) then gives

$$-\frac{1}{2\sqrt{\rho}}\partial_x^2\sqrt{\rho} + V_{\text{eff}}(\rho, x) - \omega = 0, \quad (\text{A4})$$

where the effective potential V_{eff} is

$$V_{\text{eff}}(\rho, x) = \frac{J^2}{2\rho^2} + V(x) + \frac{1}{2} \left(\eta + \frac{1}{\eta} \right) + g \frac{\rho}{\eta}. \quad (\text{A5})$$

When considering a region of homogeneous potential V , the possible homogeneous solutions are given by $V_{\text{eff}}(\rho) - \omega = 0$. To determine the number and properties of these solutions, we compute

$$\frac{dV_{\text{eff}}}{d\rho} = (1 + \rho)^{-3/2} \left(\frac{\rho}{4} + g \left(1 + \frac{\rho}{2} \right) \right) - \frac{J^2}{\rho^3}. \quad (\text{A6})$$

After multiplication by the (strictly positive for $\rho > 0$) factor ρ^3 , the right-hand side of Eq. (A6) is a monotonically increasing function of ρ , which is negative for $\rho \rightarrow 0^+$ and changes sign at a value $\rho_c > 0$ of ρ . So, $V_{\text{eff}}(\rho)$ is a monotonically decreasing function of ρ for $0 < \rho \leq \rho_c$ and an increasing function for $\rho > \rho_c$. Moreover, $V_{\text{eff}} \rightarrow \infty$ in the two limits $\rho \rightarrow 0^+$ and $\rho \rightarrow \infty$. The existence of homogeneous (or solitonic) solutions thus requires $\omega \geq V_{\text{eff}}(\rho_c)$. For $\omega > V_{\text{eff}}(\rho_c)$ there are two homogeneous solutions: a supersonic one with density $\rho_p < \rho_c$ and a subsonic one with density $\rho_b > \rho_c$ (their sup- and subsonic characters are proven in subsection A 2).

To characterize the soliton solutions, one can integrate once Eq. (A4) after multiplication by $\sqrt{\rho}\partial_x\sqrt{\rho}$. This gives

$$-\frac{1}{4}(\partial_x\sqrt{\rho})^2 - \frac{J^2}{4\rho} + \frac{V - \omega}{2}\rho + \frac{\sqrt{1 + \rho}}{2} + \frac{1}{6}(1 + \rho)^{3/2} + g\rho\sqrt{1 + \rho} - \frac{2}{3}g(1 + \rho)^{3/2} + C = 0, \quad (\text{A7})$$

where C is an integration constant. The soliton solution is then obtained by choosing C such that Eq. (A7) be satisfied for $\rho = \rho_b$ and $\partial_x\rho = 0$. The bottom of the soliton is given by the largest root ρ_s of the left-hand side of Eq. (A7)

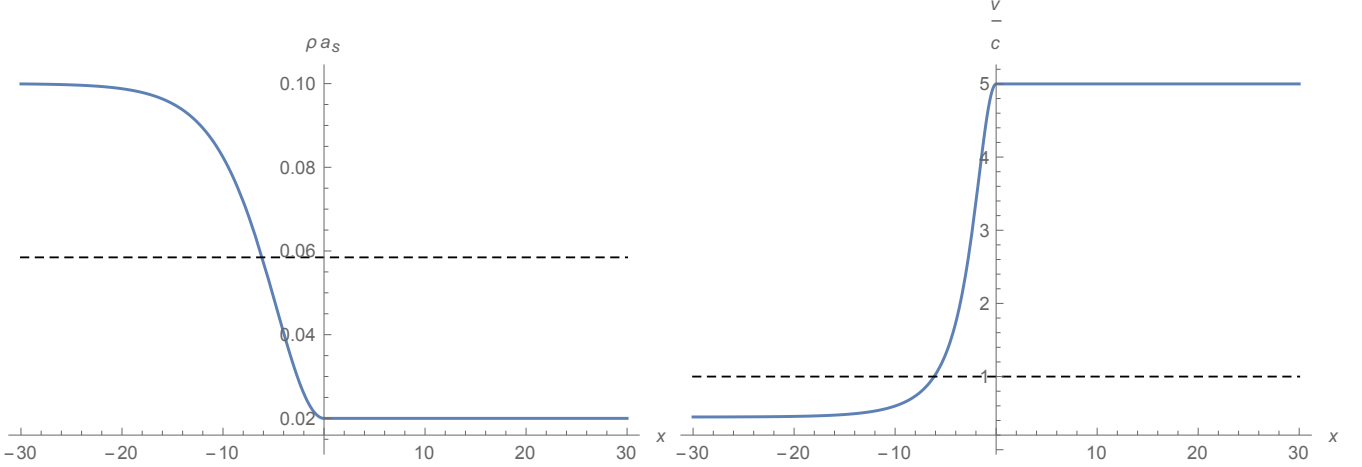


Figure 10. Plots of the local density adimensionalized by a_s (left) and Mach number (right) for the waterfall solution of the NPS Eq. (A2) in a step-like potential. The asymptotic densities ρ_{\pm} and the value of M_+ are chosen to model the flow of [1], see text. The horizontal dashed line shows the density at the horizon (left) and $M = 1$ (right). The unit of the x is $\sqrt{\hbar/(m\omega_{\perp})}$.

for $\partial_x \rho = 0$ in the interval $]0, \rho_b[$. (Its existence can be shown using that $V'_{\text{eff}}(\rho_b) > 0$ and that the left-hand side of Eq. (A7) goes to $-\infty$ for $\rho \rightarrow 0^+$.)

We now look for waterfall solutions in a step-like potential given by Eq. (5). That is, we look for a half-soliton for $x < 0$ matched with a homogeneous supersonic solution for $x > 0$. This leaves, in our non-dimensional system of units, three free parameters: g , J , and $V_- - \omega$. The value of V_+ is then fixed by imposing that $\rho_{p,+} = \rho_{s,-}$. (As in the main text, a subscript “-” (respectively “+”) denotes a quantity evaluated in the left (resp. right) region.) Alternatively, one can impose the values of the asymptotic density on each side and the asymptotic Mach number on one side. This fixes the values of the three free parameters, and thus the whole solution. From the inset of Fig. 1.b in [1] and the numerical values of the velocities reported there, we find (in our non-dimensional units) $\rho_{b,-} \approx 0.1$ and $\rho_{s,-} = \rho_{p,+} \approx 0.02$. We work with $M_+ = 5$. The corresponding flow is shown in Fig. 10. To estimate the difference with the flows obtained using the GPE, we consider the quantity

$$\chi \equiv x_H \left(\frac{dM}{dx} \right)_{x=x_H}, \quad (\text{A8})$$

where x_H is the position of the sonic horizon relative to that of the potential step. χ is proportional to the surface gravity and has no dimension; hence it is insensitive to the adimensionalization procedure and can be used to directly compare the flows obtained with the two equations. For the solution shown in Fig. 10, we obtain $\chi \approx -1.26$. By comparison, for the flow of Fig. 1 with $M_+ = 5$ we obtain $\chi \approx -1.12$.

2. Equation on linear perturbations

We now look for perturbed solutions of the form

$$\psi(x, t) = \psi_0(x, t) (1 + \phi(x, t)), \quad (\text{A9})$$

where ψ_0 is a known stationary solution with angular frequency ω_0 , local density $\rho_0 \equiv |\psi_0|^2$, and velocity $v_0 \equiv \Im((\partial_x \psi_0) / \psi_0)$. To first order in ϕ , Eq. (A2) becomes

$$i(\partial_t + v_0 \partial_x) \phi = -\frac{1}{2\rho_0} \partial_x (\rho_0 \partial_x \phi) + \frac{d}{d\rho_0} \left(V_{\text{eff}}(\rho_0) - \frac{J^2}{2\rho_0^2} \right) \rho_0 (\phi + \phi^*). \quad (\text{A10})$$

When the background flow is homogeneous, one can find a basis of solutions of the form

$$\phi(x, t) = U e^{-i\omega t + ikz} + V^* e^{i\omega^* t - ik^* z}, \quad (\text{A11})$$

where $(U, V, \omega, k) \in \mathbb{C}^4$. The angular frequency ω and wave vector k are related by the dispersion relation

$$(\omega - v_0 k)^2 = \frac{d}{d\rho_0} \left(V_{\text{eff}}(\rho_0) - \frac{J^2}{2\rho_0^2} \right) \rho_0 k^2 + \frac{k^4}{4}. \quad (\text{A12})$$

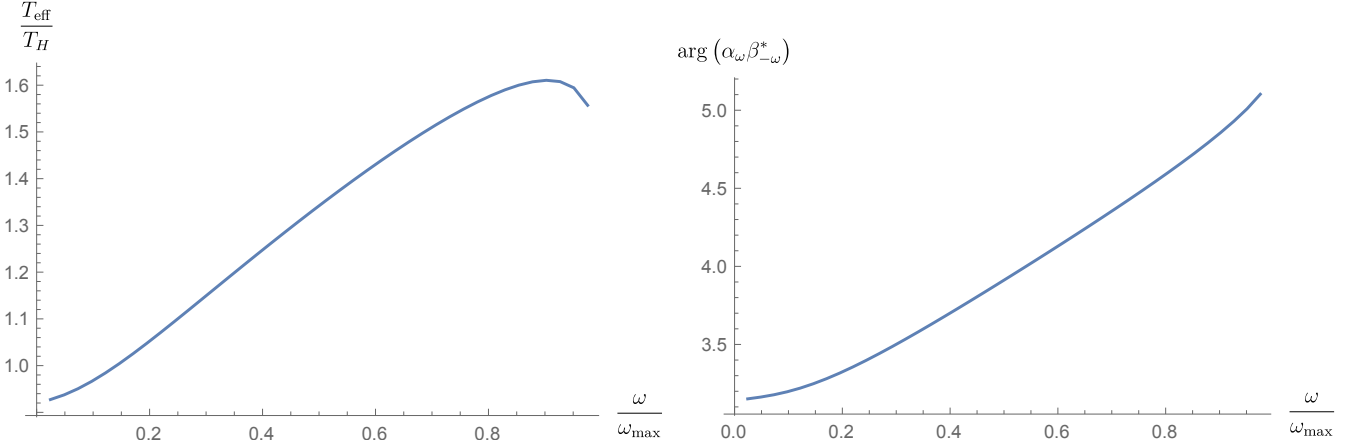


Figure 11. Effective temperature (left, in units of T_H) and relative phase of the coefficients α_ω and $\beta_{-\omega}$ (right) as functions of ω/ω_{\max} for the waterfall solution shown in Fig. 10.

The sound velocity c_0 is thus related to the background flow velocity v_0 through

$$c_0^2 - v_0^2 = V'_{\text{eff}}(\rho_0)\rho_0. \quad (\text{A13})$$

The right-hand side of Eq. (A13) is positive for $\rho_0 = \rho_b$ and negative for $\rho_0 = \rho_p$, showing that the former is subsonic while the latter is supersonic. Apart from this change in the expression of the sound velocity, Eq. (A13) is identical to the BdG equation Eq. (10). In particular, it has the same conserved scalar product and mode structure.

To characterize the deviations of the spectrum with respect to the GPE, we first compute T_H/ω_{\max} . Using the solution shown in Fig. 10, we obtain $T_H/\omega_{\max} \approx 0.065$. By comparison, for the flow corresponding to the blue curve in Fig. 1, $T_H/\omega_{\max} \approx 0.063$, i.e., smaller by about 3%. The effective temperature of Eq. (23) evaluated in the flow of Fig. 10 is shown in the left panel of Fig. 11. We observe that its behaviour closely resembles that of Fig. 3, with maximum relative deviations of a few %. The relative phase of $\beta_{-\omega}$ and α_ω , shown in the right panel, is also close to that of Fig. 9, with maximum deviations close to 0.1rad. In conclusion, although we worked here with the observed values of the asymptotic densities [1], we observed no significant deviation with respect to the results obtained when working with one-dimensional waterfall solutions.

Appendix B: Stability of the waterfall solutions

In this appendix we report numerical results confirming the stability of the waterfall solutions. We first note that the linear analysis of [19], done for the homogeneous black hole solutions with step-like profiles for both g and V , remains valid in our present setup as it only relies on the behaviour of the scattering coefficients near $\omega \rightarrow 0$ and $\omega \rightarrow \omega_{\max}$, which is the same for the homogeneous configurations considered in that reference and the waterfall ones studied here. To linear order, density perturbations thus decay polynomially in time, with an exponent equal to 3/2. The numerical results shown below confirm that this behavior remains when considering finite perturbations.

We solved the time-dependent GPE (2) starting from a perturbed waterfall configuration at $t = 0$, on a torus of radius much larger than the healing length and length scales of the initial perturbations. Explicitly, the density at $t = 0$ is

$$\rho(x, t = 0) = \left(M_+ + \frac{1 - M_+}{\cosh(\eta x)^2} + \frac{1 - M_+}{\cosh(\eta(x + x_{\max}))^2} \right) \frac{1 - \tanh(x/\epsilon)}{2} + \frac{1 + \tanh(x/\epsilon)}{2} + \delta\rho(x, 0) \quad (\text{B1})$$

where ϵ is a regulator of the order of or smaller than the step of the uniform spatial grid, x_{\max} is half the length of the integration domain (centred on $x = 0$), $\delta\rho(x, t)$ is the density perturbation, and $\eta = \sqrt{M_+^{-1} - M_+^{-2}}$. The phase

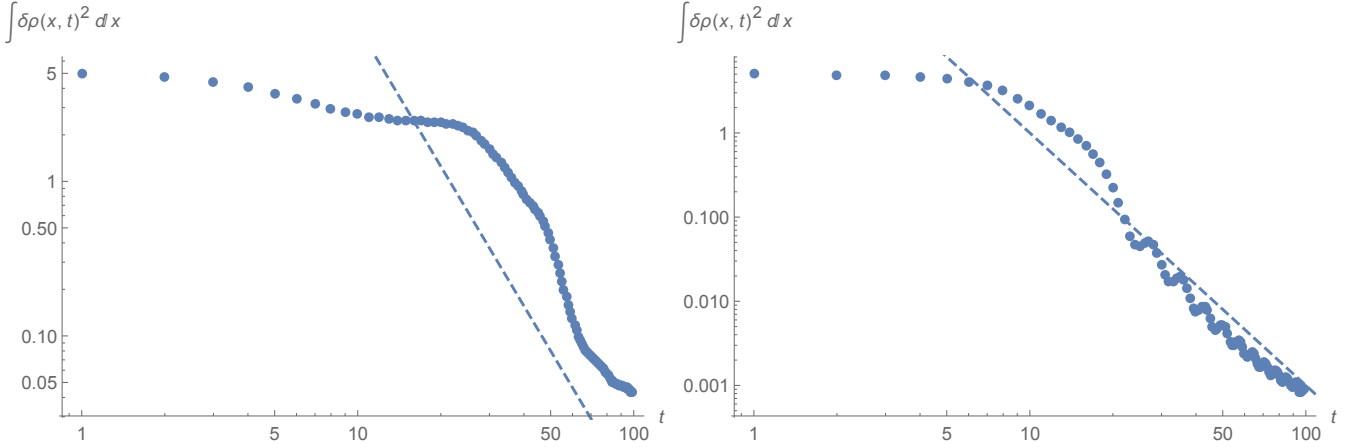


Figure 12. Integrated squared density perturbation over a waterfall solution as a function of time. The background solution is the waterfall with $M_+ = 5$. The initial perturbation has the form Eq. (B3) with $A = 1$, $\sigma = 4$, and $x_p = -20$ (left) and 20 (right). For these simulations, $x_{\max} \approx 249.5$ and the squared density perturbation is integrated between $-x_{\max}/8$ and $x_{\max}/8$. The spatial grid is made of 12800 uniformly spaced points; the time step is 0.0025. The oblique dashed lines show $10^4 t^{-3}$ (left) and $10^3 t^{-3}$ (right).

$\theta \equiv \arg \psi$ is

$$\begin{aligned} \theta(x, t=0) = & \left(\frac{x}{M_+} + \frac{M_+^{1/2} - \sqrt{M_+ - 1}}{\sqrt{2M_+ - 1 - 2\sqrt{M_+^2 - M_+}}} \arctan \left(\frac{\tanh(\eta x/2)}{\sqrt{2M_+ - 1 - 2\sqrt{M_+^2 - M_+}}} \right) \right. \\ & - \frac{M_+^{1/2} + \sqrt{M_+ - 1}}{\sqrt{2M_+ - 1 + 2\sqrt{M_+^2 - M_+}}} \arctan \left(\frac{\tanh(\eta x/2)}{\sqrt{2M_+ - 1 + 2\sqrt{M_+^2 - M_+}}} \right) \\ & + \frac{M_+^{1/2} - \sqrt{M_+ - 1}}{\sqrt{2M_+ - 1 - 2\sqrt{M_+^2 - M_+}}} \arctan \left(\frac{\tanh(\eta(x + x_{\max})/2)}{\sqrt{2M_+ - 1 - 2\sqrt{M_+^2 - M_+}}} \right) \\ & \left. - \frac{M_+^{1/2} + \sqrt{M_+ - 1}}{\sqrt{2M_+ - 1 + 2\sqrt{M_+^2 - M_+}}} \arctan \left(\frac{\tanh(\eta(x + x_{\max})/2)}{\sqrt{2M_+ - 1 + 2\sqrt{M_+^2 - M_+}}} \right) \right) \frac{1 - \tanh(x/\epsilon)}{2} \\ & + x \frac{1 + \tanh(x/\epsilon)}{2} + \delta\theta(x, 0). \end{aligned} \quad (\text{B2})$$

In Eqs. (B1) and (B2), the terms in $x + x_{\max}$ are added to implement the periodic boundary conditions; the value of x_{\max} is chosen so that $\theta(x_{\max}) - \theta(-x_{\max})$ is sufficiently close to an integer multiple of 2π to avoid large perturbations originating from $x = x_{\max}$. The configuration is thus nearly stationary for $\delta\rho = \delta\theta = 0$, and contains a black hole horizon close to $x = 0$ and a white hole horizon close to $x = x_{\max}$.

The numerical integration uses a modified version of the code of [34], written in *Mathematica* [22] with a dissipative term linear in $\delta\rho(x, t)$ $\left(\frac{|x|}{x_{\max}} - \frac{1}{2}\right)$ added in the region $|x| > x_{\max}/2$ to suppress the perturbations coming back to the black hole horizon after making a full turn. We verified that the residual waves going to the white hole horizon and back to the black hole one, as well as the part of the perturbation reflected around $x = \pm x_{\max}/2$ because of the dissipation term, are small enough not to affect the results. To estimate the evolution of the perturbations, we compute the integral of the squared density perturbation $\delta\rho$ over the interval $[-x_{\max}/8, x_{\max}/8]$ as a function of time. In Fig. 12 we show results for $M_+ = 5$ and an initial perturbation of the form

$$\delta\rho(x, 0) = A \exp \left(-(x - x_p)^2 / \sigma^2 \right), \quad \delta\theta(x, 0) = 0. \quad (\text{B3})$$

As can be seen in the figure, the integrated squared density perturbation decays as t^{-3} , in accordance with the linear theory. We verified that this behavior remains for $M_+ = 1.2, 2$, and 3.5 , as well as for similar perturbations on the phase. Although a systematic study of the domain of stability of the waterfall solutions is beyond the scope of this work, the present results indicate that they are stable both at a linear level and with respect to finite perturbations.

Appendix C: Shift of the correlations for a relativistic field

In this Appendix we study the propagation of a relativistic massless field in waterfall background flows, as well as in tanh and linear profiles. Our aim is to compute the shift with respect to the horizon (x_M of Eq. (40)) of the maximum value of the nonlocal uu -correlation function in the $x - x'$ plane. In subsection C1, we present the general calculation. In subsection C2 we consider an asymmetric tanh profile and show that, surprisingly, the shift vanishes. We then turn to two asymmetrical profiles which display a non-trivial shift: a perturbed tanh profile in C3 and a linear profile in C4.

1. Relativistic shift of the maximum of G_2

Starting from Eq. (12), we perform two simplifications. We first send the healing length to 0, as was done in Eq. (41) when sending $\lambda^2 \rightarrow 0$. We also reorder the derivatives ∂_x and x -dependent factors to work with the wave equation of a relativistic massless scalar $\phi(t, x)$. Then, because of conformal invariance, there is a complete decoupling of the v (copropagating) sector and the u sector which describes waves counterpropagating with respect to the background flow. As a result, the 2-point function G_2 is a sum of a term describing v modes (that we shall no longer discuss), and $G_{2,u}$ which describes counterpropagating waves.

The decoupling between the v and u sectors can be easily understood by considering the acoustic metric associated with the background flow [3, 4], and by rewriting it in terms of the light-like coordinates v and u :

$$ds^2 = -c^2(x)dt^2 + (dx - v(x)dt)^2 = -(c^2(x) - v^2(x))dvdu, \quad (\text{C1})$$

where

$$du \equiv dt + \frac{dx}{c(x) - v(x)}, \quad dv \equiv dt - \frac{dx}{c(x) + v(x)}. \quad (\text{C2})$$

(The signs in the definition of our light-like coordinates u and v are chosen so that lines of constant u give the characteristics of the counter-propagating waves for a flow from left to right. The differences with the standard notations come from our convention that $v(x) > 0$.)

In these settings, to obtain the Hawking radiation and its associated uu -correlation pattern, one should introduce the notion of “Unruh” vacuum [35], which is unambiguously defined as it is the only regular state across the horizon which is stationary with respect to time translations $\partial_t|_x$. In this state, at fixed t , the regularity across the sonic horizon at x_H implies that in the near vicinity of the horizon one has [25]

$$G_{2,u}(t, x; t, x') \sim \frac{-1}{4\pi} \ln |x - x'|. \quad (\text{C3})$$

In other words the regularity of the state is expressed as a translation invariance when using the regular coordinate x which is an affine coordinate at fixed t , since $ds^2 = dx^2$ at fixed t . When considered globally the 2-point function in Unruh vacuum, $G_{2,u}$ can be written as

$$G_{2,u}(u; u') = \frac{-1}{4\pi} \ln |U - U'|, \quad (\text{C4})$$

where U is a light-like coordinate which is regular across $x = x_H$, which means that $\partial_x U$ is continuous at $x = x_H$, both at fixed v and at fixed t . Up to an arbitrary scale which plays no role in the physics, U is uniquely defined by the regularity on the horizon and the stationarity of $G_{2,u}$. As we shall now see, together with the flow profile of $c(x) - v(x)$ for all values of x , this condition of regularity unambiguously fixes the shift x_M of Eq. (40).

To this end one should relate U to the two coordinates u_L, u_R which obey $du = dt + dx/(c(x) - v(x))$, and which cover respectively the left and right side of x_H . Indeed, due to the divergence of $1/(c - v)$ on the sonic horizon for $x \rightarrow x_H$, two u coordinates must be used. When integrating $du = dt + dx/(c(x) - v(x))$, the integration constant can be

chosen independently on each side of x_H . More precisely, using the fact that close to the horizon, $v - c \approx \kappa_H(x - x_H)$, one gets

$$u_{R/L} \underset{x \rightarrow x_H}{=} t + \frac{1}{\kappa_H} \ln(|x - x_H|) + C_{R/L} + o(1), \quad (\text{C5})$$

where $C_{R/L}$ are two real constants, taking a priori different values on each side of the horizon. It is convenient to adopt the conventional choice $C_L = C_R$, as it allows to express the regularity of Eq. (C4) in simple terms. Indeed, when $C_L = C_R$, one recovers the standard relation [36].

$$U = \begin{cases} \frac{1}{\kappa_H} e^{-\kappa_H u_R} & x > x_H \\ -\frac{1}{\kappa_H} e^{-\kappa_H u_L} & x < x_H \end{cases}. \quad (\text{C6})$$

Equivalently, starting with these relations, one easily verifies that the continuity of $\partial_x U$ across the horizon is equivalent to the condition $C_L = C_R$ in Eq. (C5). In the following, we work with u_R and u_L which satisfy this relation.

We remind the reader that the above exponential relation between U , specifying the regular vacuum state, and u_L which is linearly related to t and x for asymptotic values of x_L in the subsonic region encodes the steady production of thermally distributed particles at the Hawking temperature $T_H = \kappa_H/2\pi$. Similarly the symmetry under the exchange $U \rightarrow -U$, $u_L \rightarrow u_R$ encodes the correlations across the horizon between particles of opposite energy, as can be seen by studying wave packets of regular *in*-modes [5] or, equivalently, the reduction of the state due to the detection of a localized quantum on one side of the horizon [36, 37].

To relate the present formalism to density-density correlations of phonons in a transonic flow, one should consider [10]

$$G_2^{(xx)}(x, t; x', t') \equiv \frac{-1}{4\pi} \partial_x \partial_{x'} \ln(U(t, x) - U(t', x')). \quad (\text{C7})$$

At equal time, when $x < x_H$ and $x' > x_H$,

$$G_2^{(xx)} = \frac{\kappa_H^2}{16\pi} \frac{\partial_x u_R(x) \partial_{x'} u_L(x')}{\cosh^2\left(\frac{\kappa_H}{2}(u_R(x) - u_L(x'))\right)}. \quad (\text{C8})$$

Hence, in the asymptotic regions where $v - c$ becomes constant, the locus of the maxima of $G_2^{(xx)}$ gives back the mirror image null characteristics $u_R = u_L$.

To compute the shift x_M , we first assume that the coordinate u has the following asymptotic expansion:

$$u(x, t) \underset{x \rightarrow \pm\infty}{=} t + \frac{x - x_H + b_{\pm}}{v_{\pm}^{\text{gr}}} + o(1), \quad (\text{C9})$$

where $v_{\pm}^{\text{gr}} \equiv -c_{\pm} + v_{\pm}$ gives the group velocity in the laboratory frame in each asymptotic region, which satisfy $v_-^{\text{gr}} < 0$ and $v_+^{\text{gr}} > 0$. In the limit $x \rightarrow -\infty$ and $x' \rightarrow +\infty$, the maximum of $G_2^{(xx)}$ is located where

$$\frac{x - x_H + b_-}{v_-^{\text{gr}}} = \frac{x' - x_H + b_+}{v_+^{\text{gr}}}. \quad (\text{C10})$$

To get the point where these asymptotes cross each other, we set $x = x'$, giving the shift

$$\Delta x \equiv x_M - x_H = \frac{v_-^{\text{gr}} b_+ - v_+^{\text{gr}} b_-}{v_+^{\text{gr}} - v_-^{\text{gr}}}. \quad (\text{C11})$$

As expected the correction terms b_{\pm} entering in Eq. (C9) fix the shift Δx .

To complete the calculation, we now relate Δx to the profile of $c(x) - v(x)$. To this end, we use that, for $\epsilon > 0$ and $x > x_H$, and up to a global constant,

$$u_R = t + \int_{x_H + \epsilon}^x \frac{dy}{c(y) - v(y)} + \frac{1}{\kappa_H} \ln(|\epsilon|) + O(\epsilon), \quad (\text{C12})$$

while for $x < x_H$,

$$u_L = t + \int_{x_H - \epsilon}^x \frac{dy}{c(y) - v(y)} + \frac{1}{\kappa_H} \ln(|\epsilon|) + O(\epsilon). \quad (\text{C13})$$

Using these expressions and the definition of b_{\pm} Eq. (C9), we obtain

$$\frac{b_+}{v_+^{\text{gr}}} - \frac{b_-}{v_-^{\text{gr}}} = \lim_{\epsilon \rightarrow 0} \lim_{X \rightarrow \infty} \left(\int_{[x_H - X, x_H + X] - [x_H - \epsilon, x_H + \epsilon]} \frac{dx}{c(x) - v(x)} - \frac{X}{v_+^{\text{gr}}} - \frac{X}{v_-^{\text{gr}}} \right). \quad (\text{C14})$$

The near-horizon contribution is given by a principal value (and vanishes in the case one uses the near horizon approximation $c - v = -\kappa x$, which globally describes de Sitter space). The overall shift is related to the asymmetry in the ways $c - v$ approaches its asymptotic values on the two sides of the horizon.

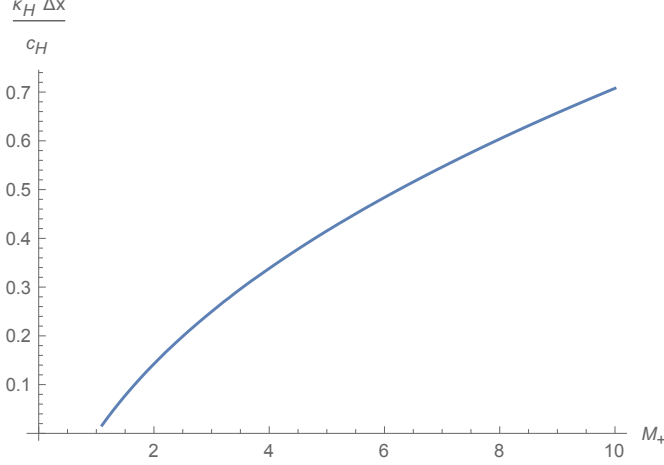


Figure 13. As a function of the downstream Mach number M_+ , we show the relativistic shift Δx of Eq. (C11) adimensionalized by the length associated with the surface gravity c_H/κ_H .

In Fig. 13, we show Δx as a function of the downstream Mach number M_+ for the waterfall solution Eq. (7), in units of c_H/κ_H . We notice that it is positive for all values of M_+ . Its behaviors at $M_+ \rightarrow 1$ and $M_+ \rightarrow \infty$ are

$$\frac{\kappa_H}{c_H} \Delta x \underset{M_+ \rightarrow 1^+}{\sim} \sqrt{\frac{2}{3}} \left(1 - \sqrt{\frac{2}{3}} \right) \operatorname{arctanh} \left(\sqrt{\frac{2}{3}} \right) (M_+ - 1), \quad (\text{C15})$$

and

$$\frac{\kappa_H}{c_H} \Delta x \underset{M_+ \rightarrow \infty}{\sim} \frac{1}{2} M_+^{1/6} \ln(M_+). \quad (\text{C16})$$

In the following we compute the same shift for tanh, perturbed tanh, and linear profiles.

2. The tanh case

We consider a profile of the form

$$c(x) - v(x) = a - b \tanh(x\sigma), \quad (\text{C17})$$

where $(a, b, \sigma) \in \mathbb{R}^3$ and $b^2 > a^2$. Eq. (C2) can be integrated explicitly, giving

$$\begin{cases} u_R = t - \frac{1}{\kappa} \left(\log \left(\frac{b \sinh(x/\sigma) - a \cosh(x/\sigma)}{b \sinh(x_R/\sigma) - a \cosh(x_R/\sigma)} \right) + \frac{a}{b} \frac{x - x_R}{\sigma} \right) \\ u_L = t - \frac{1}{\kappa} \left(\log \left(\frac{b \sinh(x/\sigma) - a \cosh(x/\sigma)}{b \sinh(x_L/\sigma) - a \cosh(x_L/\sigma)} \right) + \frac{a}{b} \frac{x - x_L}{\sigma} \right) \end{cases}, \quad (\text{C18})$$

where x_R and x_L are two integration constants. Here κ is the surface gravity, equal to

$$\kappa = \frac{b}{\sigma} \left(1 - \left(\frac{a}{b} \right)^2 \right). \quad (\text{C19})$$

Continuity of $\partial_x U$ across the horizon imposes

$$\frac{b \sinh(x_L/\sigma) - a \cosh(x_L/\sigma)}{b \sinh(x_R/\sigma) - a \cosh(x_R/\sigma)} = -\exp\left(\frac{a}{b} \frac{x_R - x_L}{\sigma}\right). \quad (\text{C20})$$

Using this relation and the position of the horizon: $x_H = (\sigma/2) \log((a+b)/(b-a))$, u_R and u_L can be written in the limits $x/\sigma \rightarrow \pm\infty$

$$\begin{cases} u_R \underset{x \rightarrow +\infty}{=} t - \frac{1}{\kappa} \left(\log\left(\frac{-\sqrt{b^2 - a^2}}{b \sinh(x_L/\sigma) - a \cosh(x_L/\sigma)}\right) - \frac{a}{2b} \log\left(\frac{b-a}{b+a}\right) - \frac{a}{b} \frac{x_L}{\sigma} + \left(1 + \frac{a}{b}\right) \frac{x - x_H}{\sigma} \right) + O(e^{-2x/\sigma}) \\ u_L \underset{x \rightarrow -\infty}{=} t - \frac{1}{\kappa} \left(\log\left(\frac{-\sqrt{b^2 - a^2}}{b \sinh(x_L/\sigma) - a \cosh(x_L/\sigma)}\right) - \frac{a}{2b} \log\left(\frac{b-a}{b+a}\right) - \frac{a}{b} \frac{x_L}{\sigma} - \left(1 - \frac{a}{b}\right) \frac{x - x_H}{\sigma} \right) + O(e^{2x/\sigma}) \end{cases} \quad (\text{C21})$$

Notice that the constant terms in u_R and u_L are the same. So, with the notations of Eq. (C9), $b_+/v_+^{\text{gr}} = b_-/v_-^{\text{gr}}$, hence a vanishing shift $\Delta x = 0$.

3. Perturbed tanh profile

The result of the subsection C2 can be misleading as they seem to suggest that the vanishing of the shift Δx is a generic property of flows with smooth $c - v$. To show that this is not the case, let us consider the following generalization of Eq. (C18):

$$u(t, x) = t + \frac{1}{\kappa} \left(\log\left(\frac{|b \sinh(x/\sigma) - a \cosh(x/\sigma) - c|}{A_0}\right) - \eta \frac{x}{\sigma} \right), \quad (\text{C22})$$

where $(a, b, c, \kappa, A_0, \eta, \sigma) \in \mathbb{R}^7$. One can check that the function U thus defined is smooth.⁵ As in subsection C2, we assume $b^2 > a^2$. One can reduce the number of free parameters by defining the non-dimensional variables

$$\bar{t} \equiv \kappa t, \bar{x} \equiv \frac{x}{\sigma} + \frac{1}{2} \log\left(\frac{b-a}{b+a}\right) \text{ and } \bar{u} \equiv \kappa u. \quad (\text{C23})$$

In the remainder of this subsection we will work only with these non-dimensional variables and remove the bars to simplify the notations. Eq. (C22) then becomes

$$u(x, t) = t + \log(|\sinh(x) - \gamma|) + \eta x, \quad (\text{C24})$$

where $\gamma \equiv c/b$. Differentiating Eq. (C24) gives

$$\frac{1}{c(x) - v(x)} = \frac{\cosh(x)}{\sinh(x) - \gamma} + \eta. \quad (\text{C25})$$

The horizon is located at $x_H = \text{argsinh}(\gamma)$. A straightforward calculation shows that $c(x) - v(x)$ has no divergence, and thus can correspond to a physical flow, if and only if

$$\eta^2 < 1 \wedge \eta\gamma < \sqrt{1 - \eta^2}. \quad (\text{C26})$$

Notice however that $c - v$ is not a monotonic function of x when $\gamma \neq 0$: $c' - v'$ changes sign at $x = \text{argsinh}(1/\gamma)$, see Fig. 14.

Setting $u(t, x) = u(t, x')$ with $x > x_H$ and $x' < x_H$ and taking the limit $x \rightarrow \infty$ gives

$$\frac{x}{v_+^{\text{gr}}} - \frac{x'}{v_-^{\text{gr}}} = 0. \quad (\text{C27})$$

⁵ Because of the absolute value, u can be continued in the complex plane to a function which is smooth just above the real axis, up to a term $i\pi/\kappa$ which arises when passing above x_H . This additional term exactly compensates the relative sign in the definition of U on both sides of the horizon, see Eq. (C6).

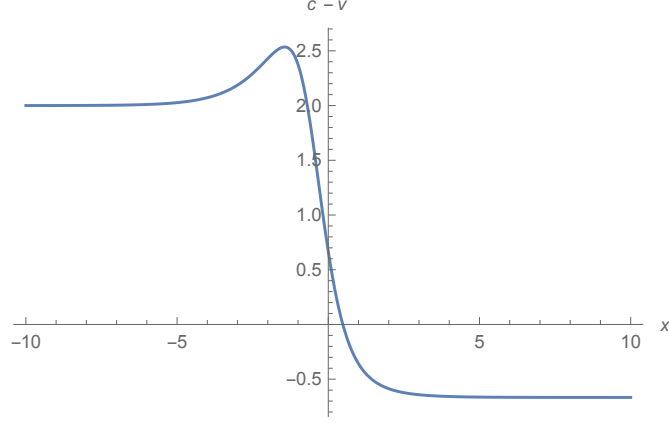


Figure 14. Profile of $c - v$ for the perturbed tanh flow of Eq. (C24) with $\gamma = \eta = 0.5$. The horizon is located at $x \approx 0.48$.

Using Eq. (C10), we get $\Delta x = -x_H$. In other words, the asymptotes of the lines $u_R = u_L$ intersect at $x_M = 0$, which is not the position of the horizon for $\gamma \neq 0$. The corresponding two-point correlation function of Eq. (C8) is shown in Fig. 15 for a positive γ . We also represent the equal-time correlation $G_2^{(tt)}$ given by

$$\begin{aligned} G_2^{(tt)}(x, t; x', t) &\equiv \frac{-1}{4\pi} \partial_t \partial_{t'} \ln (U(t, x) - U(t', x'))_{t=t'} \\ &= \frac{\kappa_H^2}{16\pi (\cosh(\frac{\kappa_H}{2}(u_R(x) - u_L(x'))))^2}, \end{aligned} \quad (\text{C28})$$

which behaves differently in the near horizon region, as it only depends on $u_R(x)$ and $u_L(x)$. Hence the maximal value of $G_2^{(tt)}(x, t; x', t)$ follows the $x(x')$ giving the image of the pair of null geodesics in the x, x' plane.

4. Linear profile

As a third example, we consider a profile of $v + c$ which is linear in a “near-horizon” region and uniform outside it. To be specific, we define three real numbers κ , $x_+ > 0$, and $x_- < 0$, and choose the profile

$$c(x) - v(x) = \begin{cases} -\kappa x_- & x < x_- \\ -\kappa x & x_- \leq x \leq x_+ \\ -\kappa x_+ & x_+ < x \end{cases}. \quad (\text{C29})$$

κ is then the surface gravity. Integrating $1/(c - v)$ over x , imposing that U be a smooth function of x across the horizon and at $x \in \{x_-, x_+\}$ gives

$$u(x) = \begin{cases} t - \frac{x - x_-}{\kappa x_-} - \frac{1}{\kappa} \log\left(\frac{-x_-}{|x_0|}\right) & x < x_- \\ t - \frac{1}{\kappa} \log\left(\left|\frac{x}{x_0}\right|\right) & x_- \leq x \leq x_+ \\ t - \frac{x - x_+}{\kappa x_+} - \frac{1}{\kappa} \log\left(\frac{x_+}{|x_0|}\right) & x_+ < x \end{cases}, \quad (\text{C30})$$

where x_0 is an arbitrary integration constant. Considering two points $x > x_+$ and $x' < x_-$, setting $u(t, x) = u(t, x')$ gives

$$\frac{x}{\kappa x_+} - \frac{x'}{\kappa x_-} = \frac{1}{\kappa} \log\left(\frac{-x_-}{x_+}\right). \quad (\text{C31})$$

Since the horizon is at $x_H = 0$, we obtain

$$\Delta x = \frac{\log(-x_-/x_+)}{(1/x_+) - (1/x_-)}. \quad (\text{C32})$$

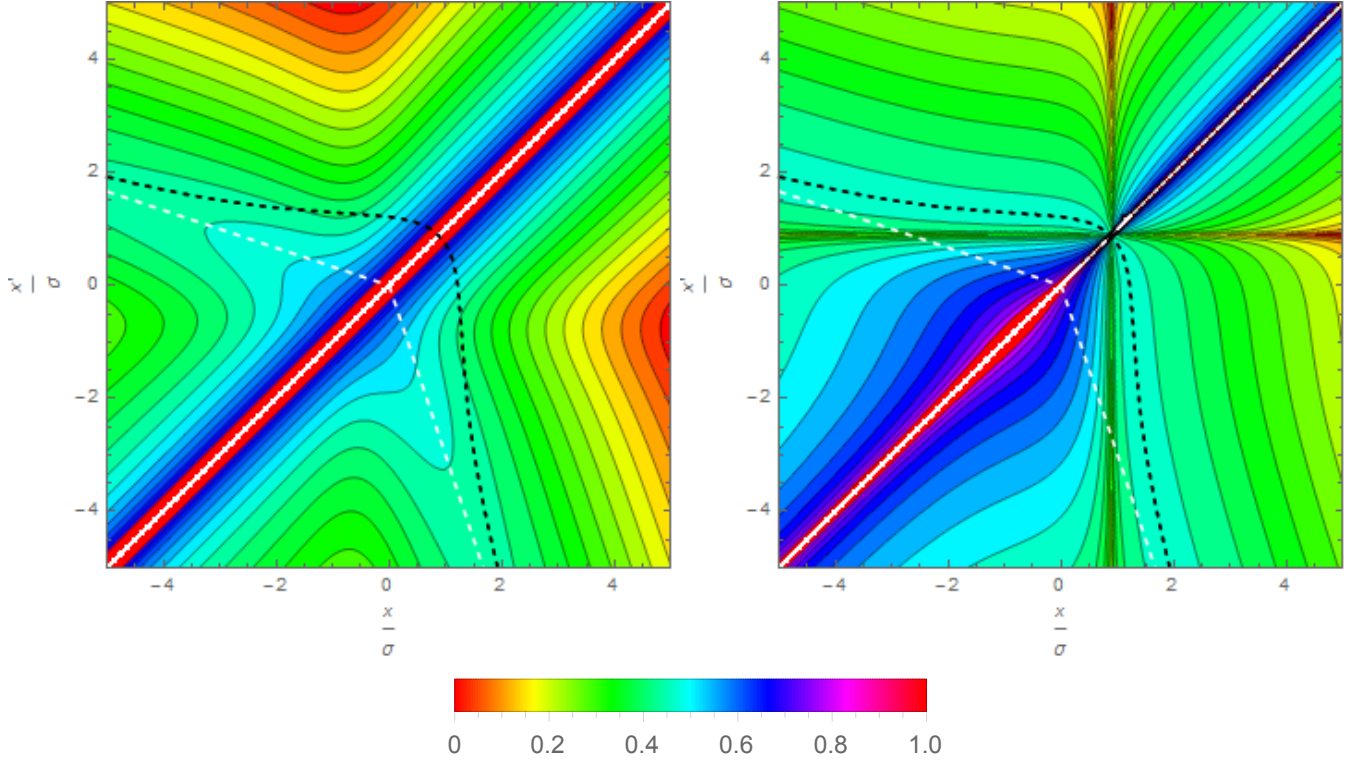


Figure 15. Two-point correlation function Eq. (C7) (left) and Eq. (C28) (right) (rescaled so that the maximum represented value is 1) for a perturbed tanh profile given by Eq. (C25), with $\gamma = 2\eta = 1$. The black, dashed line shows the locus $u_R(x) = u_L(x')$ and $u_L(x) = u_R(x')$. The white, straight, dashed half-lines are their asymptotes. In these plots, the origin of x has been put where they meet, i.e., $x_M = 0$. Hence the sonic horizon is located at $x_H = -\Delta x$. On the right plot, we clearly see that the maxima of $G_2^{(tt)}$, which give $x(x')$, start from $x = x_H$. On the left plot, we see that the maxima of $G_2^{(xx)}$ emerge from a broad region which is approximately centered on $x_M = 0$, and not on x_H .

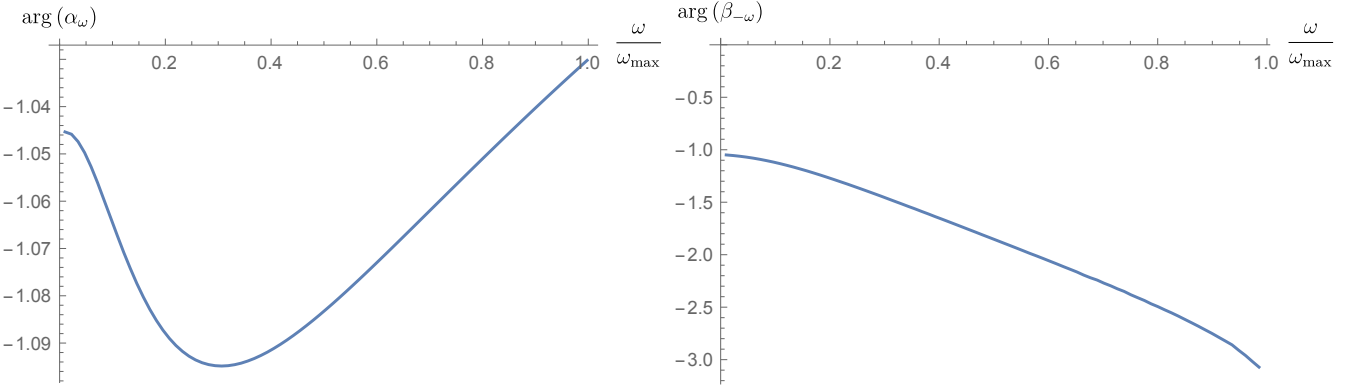


Figure 16. Phase of the scattering coefficients α_ω (left) and $\beta_{-\omega}$ (right) as defined in the main text (see discussion above Eq. (39)) for the waterfall solution with $M_+ = 5$.

Appendix D: Phase of the coefficients α_ω and β_ω

In this appendix we consider the phases of the individual coefficients α_ω and $\beta_{-\omega}$. When working with thermal states or with the vacuum, it is unclear whether these phases can be measured experimentally. However they can certainly be measured when working in the stimulated regime by sending a classical wave [23, 38, 39], or a coherent state [7], towards the horizon. We hope they will be measured in forthcoming experiments based on water waves.

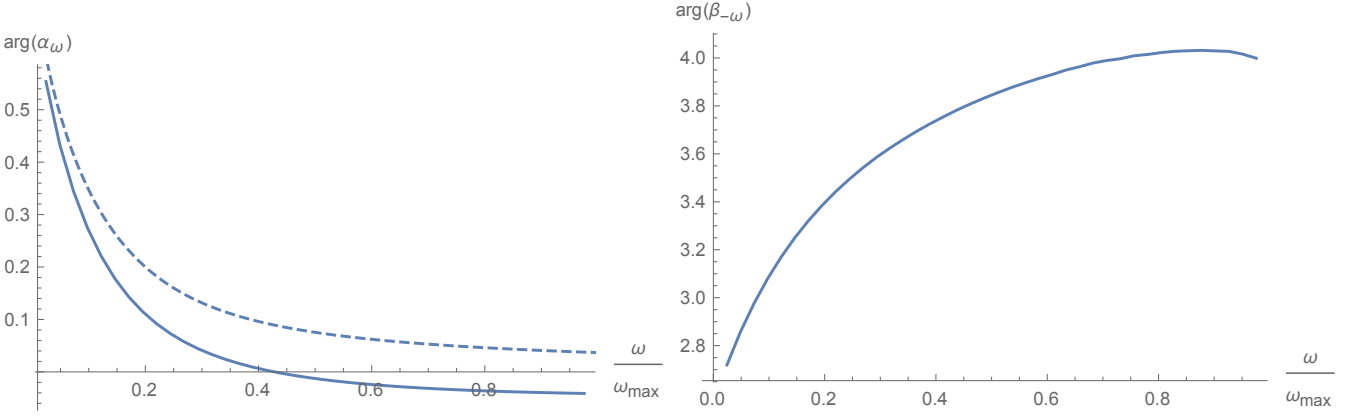


Figure 17. Phase of the scattering coefficients α_ω (left) and $\beta_{-\omega}$ (right) defined using Eq. (D1) for the waterfall solution with $M_+ = 5$. The dashed curve shows the phase obtained from Eq. (76) in [40].

We first show in Fig. 16 the phases $\arg \alpha_\omega$ and $\arg \beta_{-\omega}$ for the waterfall with M_+ which are obtained using the definition of the asymptotic modes detailed in the main text. Fig. 17 shows their modified values when the phases of the asymptotic modes are given by their WKB approximations:

$$\begin{aligned} \arg \left(\phi_{-\omega}^{d,\text{WKB}}(x) \right)_{x \rightarrow +\infty} &= \int_{x_{\text{tp}}(-\omega)}^x k_{-\omega}^d(y) dy, \quad \arg \left(\phi_{-\omega}^{u,\text{WKB}}(x) \right)_{x \rightarrow -\infty} = \int_{x_{\text{tp}}(-\omega)}^x k_{-\omega}^u(y) dy, \\ \text{and } \arg \left(\phi_\omega^{u,\text{WKB}}(x) \right)_{x \rightarrow +\infty} &= \int_{x_{\text{tp}}(-\omega)}^x k_\omega^u(y) dy. \end{aligned} \quad (\text{D1})$$

In the above $x_{\text{tp}}(-\omega)$ is the turning point of the characteristic of frequency $-\omega$. It is located in the supersonic region. Because there are two branches for $-\omega < 0$, the superscripts u and d indicate whether one uses the hydrodynamical root or the dispersive root. When considering the positive frequency mode, there is no ambiguity since there is a single root k_ω for all values of x . Similar WKB modes furnish an appropriate mode basis to compute analytically the norm and the phases of the scattering coefficients, see [40]. The comparison with the analytical prediction is made for $\arg \alpha_\omega$ on the left panel. The agreement is rather good. Further work is needed to perform the same comparison for $\arg \beta_{-\omega}$.

[1] J. Steinhauer, “Observation of thermal Hawking radiation and its entanglement in an analogue black hole,” (2015), [arXiv:1510.00621 \[gr-qc\]](https://arxiv.org/abs/1510.00621).

[2] L. P. Pitaevskii and S. Stringari, *Bose-Einstein Condensation*, International Series of Monographs on Physics (Clarendon Press, 2003).

[3] W. G. Unruh, “Experimental black hole evaporation,” *Phys. Rev. Lett.* **46**, 1351–1353 (1981).

[4] W. G. Unruh, “Sonic analog of black holes and the effects of high frequencies on black hole evaporation,” *Phys. Rev. D* **51**, 2827–2838 (1995).

[5] R. Brout, S. Massar, R. Parentani, and P. Spindel, “Hawking radiation without transPlanckian frequencies,” *Phys. Rev. D* **52**, 4559–4568 (1995), [arXiv:hep-th/9506121 \[hep-th\]](https://arxiv.org/abs/hep-th/9506121).

[6] S. Corley and T. Jacobson, “Hawking spectrum and high frequency dispersion,” *Phys. Rev. D* **54**, 1568–1586 (1996), [arXiv:hep-th/9601073 \[hep-th\]](https://arxiv.org/abs/hep-th/9601073).

[7] J. Macher and R. Parentani, “Black hole radiation in Bose-Einstein condensates,” *Phys. Rev. A* **80**, 043601 (2009), [arXiv:0905.3634 \[cond-mat.quant-gas\]](https://arxiv.org/abs/0905.3634).

[8] L. J. Garay, J. R. Anglin, J. I. Cirac, and P. Zoller, “Black holes in Bose-Einstein condensates,” *Phys. Rev. Lett.* **85**, 4643–4647 (2000), [arXiv:gr-qc/0002015 \[gr-qc\]](https://arxiv.org/abs/gr-qc/0002015).

[9] P. E. Larre, A. Recati, I. Carusotto, and N. Pavloff, “Quantum fluctuations around black hole horizons in Bose-Einstein condensates,” *Phys. Rev. A* **85**, 013621 (2012), [arXiv:1110.4464 \[cond-mat.quant-gas\]](https://arxiv.org/abs/1110.4464).

[10] R. Balbinot, A. Fabbri, S. Fagnocchi, A. Recati, and I. Carusotto, “Non-local density correlations as signal of Hawking radiation in BEC acoustic black holes,” *Phys. Rev. A* **78**, 021603 (2008), [arXiv:0711.4520 \[cond-mat.other\]](https://arxiv.org/abs/0711.4520).

[11] I. Carusotto, S. Fagnocchi, A. Recati, R. Balbinot, and A. Fabbri, “Numerical observation of Hawking radiation from acoustic black holes in atomic BECs,” *New J. Phys.* **10**, 103001 (2008), [arXiv:0803.0507 \[cond-mat.other\]](https://arxiv.org/abs/0803.0507).

- [12] D. Campo and R. Parentani, “Inflationary spectra and violations of Bell inequalities,” *Phys. Rev.* **D74**, 025001 (2006), [arXiv:astro-ph/0505376 \[astro-ph\]](https://arxiv.org/abs/astro-ph/0505376).
- [13] J. R. M. de Nova, F. Sols, and I. Zapata, “Violation of Cauchy-Schwarz inequalities by spontaneous Hawking radiation in resonant boson structures,” *Phys. Rev.* **A89**, 043808 (2014), [arXiv:1211.1761 \[cond-mat.quant-gas\]](https://arxiv.org/abs/1211.1761).
- [14] X. Busch and R. Parentani, “Quantum entanglement in analogue Hawking radiation: When is the final state nonseparable?” *Phys. Rev.* **D89**, 105024 (2014), [arXiv:1403.3262 \[gr-qc\]](https://arxiv.org/abs/1403.3262).
- [15] D. Boiron, A. Fabbri, P. É. Larré, N. Pavloff, C. I. Westbrook, and P. Zin, “Quantum signature of analog Hawking radiation in momentum space,” *Phys. Rev. Lett.* **115**, 025301 (2015), [arXiv:1406.5229 \[cond-mat.quant-gas\]](https://arxiv.org/abs/1406.5229).
- [16] J. Steinhauer, “Measuring the entanglement of analogue Hawking radiation by the density-density correlation function,” *Phys. Rev.* **D92**, 024043 (2015), [arXiv:1504.06583 \[gr-qc\]](https://arxiv.org/abs/1504.06583).
- [17] J. R. M. de Nova, F. Sols, and I. Zapata, “Entanglement and violation of classical inequalities in the Hawking radiation of flowing atom condensates,” *New J. Phys.* **17**, 105003 (2015), [arXiv:1509.02224 \[cond-mat.quant-gas\]](https://arxiv.org/abs/1509.02224).
- [18] J. Macher and R. Parentani, “Black/White hole radiation from dispersive theories,” *Phys. Rev.* **D79**, 124008 (2009), [arXiv:0903.2224 \[hep-th\]](https://arxiv.org/abs/0903.2224).
- [19] F. Michel, R. Parentani, and R. Zegers, “No hair theorems for analogue black holes,” *Phys. Rev.* **D93**, 065039 (2016), [arXiv:1511.05289 \[cond-mat.quant-gas\]](https://arxiv.org/abs/1511.05289).
- [20] S. Finazzi and R. Parentani, “On the robustness of acoustic black hole spectra,” *Proceedings, Spanish Relativity Meeting: Gravity as a crossroad in physics (ERE 2010)*, *J. Phys. Conf. Ser.* **314**, 012030 (2011), [arXiv:1102.1452 \[gr-qc\]](https://arxiv.org/abs/1102.1452).
- [21] S. Finazzi and R. Parentani, “Hawking radiation in dispersive theories, the two regimes,” *Phys. Rev.* **D85**, 124027 (2012), [arXiv:1202.6015 \[gr-qc\]](https://arxiv.org/abs/1202.6015).
- [22] Wolfram Research Inc., *Mathematica 7.0* (2008).
- [23] L. P. Euv, F. Michel, R. Parentani, T. G. Philbin, and G. Rousseaux, “Observation of noise correlated by the Hawking effect in a water tank,” (2015), [arXiv:1511.08145 \[physics.flu-dyn\]](https://arxiv.org/abs/1511.08145).
- [24] C. Mayoral, A. Recati, A. Fabbri, R. Parentani, R. Balbinot, and I. Carusotto, “Acoustic white holes in flowing atomic Bose-Einstein condensates,” *New J. Phys.* **13**, 025007 (2011), [arXiv:1009.6196 \[cond-mat.quant-gas\]](https://arxiv.org/abs/1009.6196).
- [25] R. Parentani, “From vacuum fluctuations across an event horizon to long distance correlations,” *Phys. Rev.* **D82**, 025008 (2010), [arXiv:1003.3625 \[gr-qc\]](https://arxiv.org/abs/1003.3625).
- [26] D. Campo and R. Parentani, “Inflationary spectra and partially decohered distributions,” *Phys. Rev.* **D72**, 045015 (2005), [arXiv:astro-ph/0505379 \[astro-ph\]](https://arxiv.org/abs/astro-ph/0505379).
- [27] J. Adamek, X. Busch, and R. Parentani, “Dissipative fields in de Sitter and black hole spacetimes: quantum entanglement due to pair production and dissipation,” *Phys. Rev.* **D87**, 124039 (2013), [arXiv:1301.3011 \[hep-th\]](https://arxiv.org/abs/1301.3011).
- [28] A. Coutant and R. Parentani, “Undulations from amplified low frequency surface waves,” *Phys. Fluids* **26**, 044106 (2014), [arXiv:1211.2001 \[physics.flu-dyn\]](https://arxiv.org/abs/1211.2001).
- [29] X. Busch, F. Michel, and R. Parentani, “Suppression of infrared instability in transsonic flows by condensation of zero-frequency short wave length phonons,” *Phys. Rev.* **D90**, 105005 (2014), [arXiv:1408.2442 \[gr-qc\]](https://arxiv.org/abs/1408.2442).
- [30] I. Carusotto, R. Balbinot, A. Fabbri, and A. Recati, “Density correlations and dynamical Casimir emission of Bogoliubov phonons in modulated atomic Bose-Einstein condensates,” *Eur. Phys. J.* **D56**, 391–404 (2010), [arXiv:0907.2314 \[cond-mat.quant-gas\]](https://arxiv.org/abs/0907.2314).
- [31] X. Busch and R. Parentani, “Dynamical Casimir effect in dissipative media: When is the final state nonseparable?” *Phys. Rev.* **D88**, 045023 (2013), [arXiv:1305.6841 \[cond-mat.quant-gas\]](https://arxiv.org/abs/1305.6841).
- [32] L. Salasnich, A. Parola, and L. Reatto, “Effective wave equations for the dynamics of cigar-shaped and disk-shaped Bose condensates,” *Phys. Rev. A* **65**, 043614 (2002), [cond-mat/0201395](https://arxiv.org/abs/cond-mat/0201395).
- [33] M. Tettamanti, S. L. Cacciatori, A. Parola, and I. Carusotto, “Numerical study of a recent black hole lasing experiment,” (2016), [arXiv:1603.04702 \[cond-mat.quant-gas\]](https://arxiv.org/abs/1603.04702).
- [34] F. Michel and R. Parentani, “Nonlinear effects in time-dependent transonic flows: An analysis of analog black hole stability,” *Phys. Rev.* **A91**, 053603 (2015), [arXiv:1502.04679 \[gr-qc\]](https://arxiv.org/abs/1502.04679).
- [35] W. G. Unruh, “Notes on black hole evaporation,” *Phys. Rev.* **D14**, 870 (1976).
- [36] R. Brout, S. Massar, R. Parentani, and Ph. Spindel, “A Primer for black hole quantum physics,” *Phys. Rept.* **260**, 329–454 (1995), [arXiv:0710.4345 \[gr-qc\]](https://arxiv.org/abs/0710.4345).
- [37] S. Massar and R. Parentani, “From vacuum fluctuations to radiation. 2. Black holes,” *Phys. Rev.* **D54**, 7444–7458 (1996).
- [38] G. Rousseaux, C. Mathis, P. Maissa, T. G. Philbin, and U. Leonhardt, “Observation of negative phase velocity waves in a water tank: A classical analogue to the Hawking effect?” *New J. Phys.* **10**, 053015 (2008), [arXiv:0711.4767 \[gr-qc\]](https://arxiv.org/abs/0711.4767).
- [39] S. Weinfurtner, E. W. Tedford, M. C. J. Penrice, W. G. Unruh, and G. A. Lawrence, “Measurement of stimulated Hawking emission in an analogue system,” *Phys. Rev. Lett.* **106**, 021302 (2011), [arXiv:1008.1911 \[gr-qc\]](https://arxiv.org/abs/1008.1911).
- [40] A. Coutant, R. Parentani, and S. Finazzi, “Black hole radiation with short distance dispersion, an analytical S-matrix approach,” *Phys. Rev.* **D85**, 024021 (2012), [arXiv:1108.1821 \[hep-th\]](https://arxiv.org/abs/1108.1821).